Atomistic Simulations of 40 Ar Diffusion in Muscovite

Jehiel Nteme, Stéphane Scaillet, Pascal Brault, Laurent Tassan-Got

Journal Pre-proofs

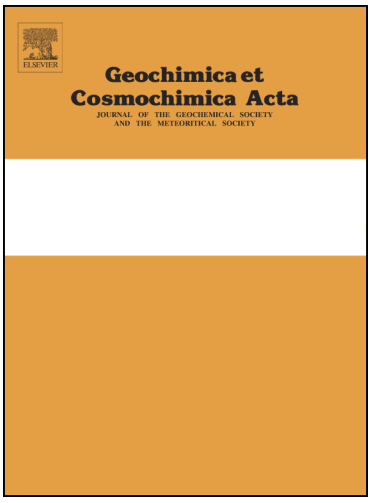

Atomistic Simulations of ^{40}Ar Diffusion in Muscovite

Jehiel Nteme, Stéphane Scaillet, Pascal Brault, Laurent Tassan-Got

PII: S0016-7037(22)00219-8
DOI: https://doi.org/10.1016/j.gca.2022.05.004
Reference: GCA 12646

To appear in: *Geochimica et Cosmochimica Acta*

Received Date: 4 December 2021
Accepted Date: 2 May 2022

Please cite this article as: Nteme, J., Scaillet, S., Brault, P., Tassan-Got, L., Atomistic Simulations of ^{40}Ar Diffusion in Muscovite, *Geochimica et Cosmochimica Acta* (2022), doi: https://doi.org/10.1016/j.gca.2022.05.004

Atomistic Simulations of ^{40}Ar Diffusion in Muscovite

Jehiel Nteme[a,b,*], Stéphane Scaillet[a], Pascal Brault[b], Laurent Tassan-Got[c,d]

[a] *Univ. Orléans, CNRS, BRGM, Institut des Sciences de la Terre d'Orléans (ISTO), UMR 7327, F-45071, Orléans, France*
[b] *Univ. Orléans, CNRS, Groupe de Recherches sur l'Energétique des Milieux Ionisés (GREMI), UMR 7344, 45067 Orléans, France*
[c] *Université Paris-Saclay, CNRS, IN2P3, Laboratoire de Physique des deux infinis Irène Joliot-Curie (IJCLab), 91405 Orsay, France*
[d] *Conseil Européen pour la Recherche Nucléaire (CERN), Espl. des Particules 1, 1211 Meyrin, Geneva, Switzerland*

Abstract

Muscovite ranks among the most commonly dated minerals in ^{40}Ar/^{39}Ar geochronology. Yet, its use in thermochronological reconstructions is hampered by the lack of reliable data on its ^{40}Ar diffusional behavior. In this contribution, we investigate ^{40}Ar lattice diffusion in muscovite at the atomic scale using Molecular Dynamics (MD) simulations combined with Nudged Elastic Band (NEB) and Transition State Theory (TST). Classical MD simulations of ^{40}Ar recoil dynamics in $2M_1$ muscovite reveal that ^{40}Ar initially resides predominantly in the interlayer region, close to its production site. Systematic computations of migration barriers coupling NEB with TST identify the divacancy mechanism as the more energetically favorable pathway for ^{40}Ar diffusion in the interlayer region, with characteristic enthalpy of motion $E = 66$ kcal.mol^{-1} and vibrational entropy term $D_0 = 6 \times 10^{-4}$ cm^2.s^{-1}. For typical cooling rates between 1−100 °C.Ma^{-1} and grain size varying from 0.1 and 1 mm, these parameters predict closure temperatures significantly higher ($\sim$ 200 °C) than currently accepted maximum estimates ($\sim$ 500 °C). Consistent with long-standing empirical evidence, our theoretical results downplay the role of purely thermally activated diffusion in promoting efficient ^{40}Ar transport in ideal (stoichiometrically stable and undefective) muscovite. Along with experimental and field-based evidence, they call for more complex physics to explain the ^{40}Ar retention properties of natural muscovite, most notably by considering crystal-chemical disequilibrium interactions and the reactivity of the interlayer with the external medium.

Keywords: ^{40}Ar diffusion, Muscovite, Molecular Dynamics, Transition State Theory, Thermochronology

*Corresponding author
Email address: jehiel.nteme-mukonzo@univ-orleans.fr (Jehiel Nteme)

1. Introduction

Diffusion is the main mechanism governing atomic transport in minerals. It is fundamental to the understanding of many geological processes in terms of kinetics of metamorphic transformations and closure behavior of radio-isotopic systems (Dodson, 1973). Among these, the $^{40}Ar/^{39}Ar$ dating technique has been widely applied for studying Earth processes in the thermal range controlling the retention behavior of $^{40}Ar-$bearing minerals (McDougall and Harrison, 1999). Being non bonded, ^{40}Ar is expected to be much more mobile than silicate-forming elements and therefore much more sensitive to thermal effects. The commonly observed discordance between for example $^{40}Ar/^{39}Ar$ and U/Pb ages has been attributed to the fact that common minerals lose their ^{40}Ar at crustal medium to moderate temperatures, giving apparent $^{40}Ar/^{39}Ar$ ages that do not reflect the time of crystallization but the time when the mineral was sufficiently cold to become effectively closed to ^{40}Ar loss by diffusion (Hart, 1960; Armstrong, 1966). Such a closed-system behavior has been theoretized in terms of a physically defined closure temperature (T_c) taking into account the Arrhenian dependence of intracrystalline (lattice) diffusion to temperature according to (Dodson, 1973):

$$T_c = \frac{E}{R \ln \left(\frac{A R T_c^2 D_0 / a^2}{E \, dT/dt} \right)} \tag{1}$$

in which E is the activation energy and D_0 the pre-exponential factor. dT/dt is the cooling rate, a the diffusion radius, A a numerical constant appropriate for the chosen geometry for diffusion, and R the gas constant. This expression emphasizes the importance of the diffusion parameters E and D_o in any quantitative interpretation of $^{40}Ar/^{39}Ar$ metamorphic ages in terms of thermal-kinetic crustal processes.

Among those minerals commonly dated by $^{40}Ar/^{39}Ar$, muscovite stands apart due to its high potassium content and ubiquity in most crustal lithologies, all the way down from the epizone to subduction-zone metamorphic conditions (McDougall and Harrison, 1999). However, the ^{40}Ar diffusion behavior in muscovite remains poorly understood. Early on, maximum retention temperatures of ca. 350 °C to as high as 400 °C (or greater) were inferred from field calibration of apparent ages vs. metamorphic grade (Purdy and Jäger, 1976)

and pioneering diffusion experiments (Hart, 1960). Other ^{40}Ar diffusivity estimates were later proposed by Hames and Bowring (1994), Lister and Baldwin (1996) and Kirschner et al. (1996). Hames and Bowring (1994) and Lister and Baldwin (1996) re-evaluated the early thermal-hydrothermal experimental data of Robbins (1972) to suggest the values $E = 52$ kcal.mol^{-1} and $D_0 = 0.04$ cm^2.s^{-1} (Hames and Bowring, 1994), and $E = 41.8$ kcal.mol^{-1} and $D_0 = 3.352 \times 10^{-7}$ cm^2.s^{-1} (Lister and Baldwin, 1996). Kirschner et al. (1996) inferred an activation energy of $E = 58$ kcal.mol^{-1} with $D_0 = 0.24$ cm^2.s^{-1} from an empirical thermal model binned to ^{40}Ar/^{39}Ar ages in muscovites grown during nappe thrusting in the Western Alps. Nowadays, commonly adopted values are those determined by Harrison et al. (2009) from hydrothermal experiments conducted in the range 730-600 °C and $P = 10$, 20 kbar ($E = 63$ kcal.mol^{-1}; $D_0 = 2.3$ cm^2.s^{-1}). Some other estimates were inferred by Forster and Lister (2014) and Lister and Forster (2016) using in vacuo experiments ($E = 67$ kcal.mol^{-1} and $D_0/a^2 = 1.2 \times 10^9$ s^{-1}).

These parameters imply theoretical ^{40}Ar-closure temperatures lower than 500 °C (Harrison et al. 2009). However, cases of effective ^{40}Ar retention have been consistently reported for muscovites exposed to temperatures in excess of this value (Monié, 1990; Scaillet et al., 1990, 1992; Monié and Chopin, 1991; Arnaud and Kelley, 1995; Scaillet, 1996; Di Vincenzo et al., 2001, 2004, 2006; Balogh and Dunkl, 2005; Hames et al., 2008; Itaya et al., 2009; Allaz et al., 2011; Beltrando et al., 2013; Halama et al., 2014; Schertl and Hammerschmidt, 2016; Laurent et al., 2021). While most of these studies relate to high-pressure phengites from eclogite-facies rocks for which the combined effect of pressure and composition (e.g., Tschermak substitution) may have influenced the ^{40}Ar diffusion behavior (Wijbrans and Mcdougall, 1986; Scaillet et al., 1992; Scaillet, 1998), a high retentivity has also been suggested in other settings for which compositional and pressure effects are not prevalent (Di Vincenzo et al., 2004; Hames et al., 2008; Itaya et al., 2009; Allaz et al., 2011). The discordance between experimental predictions and geologic evidence raises the fundamental question as to the meaning of such ^{40}Ar/^{39}Ar ages: Do they reflect cooling or (re)crystallization? The answer requires a better understanding of the ^{40}Ar diffusion behavior in muscovite as a function of several parameters including temperature, chemical composition, and other intensive variables such as pressure.

In this work, we focus on the ^{40}Ar diffusional behavior in muscovite with respect to temperature. Unlike previous studies that investigated the ^{40}Ar diffusivity in muscovite experimentally and empirically, we re-evaluate the ^{40}Ar diffusion dependence to temperature via atomistic simulations. These simulations, which include various methods (e.g., Density Functional Theory − DFT, Molecular Dynamics − MD, Kinetic Monte-Carlo − KMC, etc.), show many advantages over laboratory experiments. While the determination of rare-gas diffusivities in hydrothermal experiments is based on finite-state observables (fractional loss), atomistic simulations investigate the diffusion behavior at the atomic scale, allowing the identification and characterization of the diffusion mechanism (e.g., interstitial vs. vacancy mechanism) apt to explain the bulk migration of the diffusing species across the crystal. Also, atomistic simulations permit to analyze the diffusion process in a perfect lattice structure, unlike laboratory experiments that use natural crystals which commonly contain impurities and microstructural defects.

Atomistic simulations have been widely applied to the study of solid-state diffusion in the field of Material Science. Quite recently, they have been used for the theoretical characterization of low-temperature (fast-diffusing) thermochronometers like He and Ne in hematite, goethite, zircon, apatite and quartz via a multi-scale approach combining DFT with KMC (Saadoune et al., 2009; Bengston et al., 2012; Djimbi et al., 2015; Balout et al., 2017a,b; Gerin et al., 2017; Bassal et al., 2020; Domingos et al., 2020; Gautheron et al., 2020). DFT simulations of rare-gas (He, Ne, Ar, Kr, Xe) diffusion in hydrated minerals have further been applied to quantify the efficiency of noble gas recycling in subduction zones (Wang et al., 2020). DFT has also been successfully used to constrain He diffusion in olivine, quartz and coesite at mantle pressures (Wang et al., 2015; Liu et al., 2021). In this paper, we investigate ^{40}Ar diffusion in muscovite by combining MD with TST. Our results reveal ^{40}Ar diffusion kinetics several orders of magnitude slower than current estimates.

2. Methods

2.1. Crystal structure model

The crystal structure of muscovite [$KAl_2(Si_3Al)O_{10}(OH)_2$] consists of a stacking of tetrahedral - octahedral - tetrahedral (T−O−T) layers held together across the interlayer space

by K^+ ions, which compensate the negative structural charge resulting from the substitution of Al for Si (Bailey, 1984). Tetrahedral silicon layers and dioctahedral aluminum layers are connected through bridging oxygens. In this work, we use a $2M_1$ muscovite atomic model based on the structural data of Catti et al. (1989). The model consists of a periodic supercell of $6 \times 3 \times 1$ unit cells along the crystallographic directions a, b, and c, respectively (Fig. 1a). Tetrahedral Al atoms are distributed in an irregular pattern while obeying the short range Lowenstein rule (Loewenstein, 1954) and the principle of local charge balance (Herrero et al., 1985, 1987). Accordingly, no ^{IV}Al−O−^{IV}Al bond was allowed and each hexagonal tetrahedral ring contains either one or two Al atoms (Fig. 1b). Each K^+ is located between one Si_4Al_2 ring and one Si_5Al_1 ring to ensure an equitable charge distribution.

2.2. Computational details

Classical Molecular dynamics (MD) consists in simulating the trajectory of a system of interacting particles (atoms and/or molecules) over time by solving Newton's equations of motion (Frenkel and Smith, 2002; Rapaport, 2004). Interatomic interactions are computed based on force fields, which are parameterized using experimental results or *ab initio* simulations. We performed MD simulations using the simulation package LAMMPS (Thompson et al., 2021). The interatomic interactions were computed using ClayFF, a non-reactive force field that describes hydrated mineral systems through essentially nonbonded potentials (Cygan et al., 2004). Since its development, this force field has been widely used in MD simulations of phyllosilicates and other common minerals for which it has been shown to faithfully reproduce the structure and many thermodynamic properties (Greathouse et al., 2005, 2006; Kirkpatrick et al., 2005; Padma et al., 2006; Larentzos et al., 2007; Liu et al., 2007, 2008; Kerisit et al., 2008; Meleshyn, 2008; Wander and Clark, 2008; Cygan et al., 2009; Malani et al., 2009; Ferrage et al., 2010; Kalinichev et al., 2010; Tao et al., 2010; Argyris et al., 2011a,b; Ho et al., 2011; Teich-McGoldrick et al., 2012; Churakov, 2013; Loganathan and Kalinichev, 2013; Morrow et al., 2013). The pairwise energy for atoms i and j separated by a distance r_{ij} is given by

$$E_{ij} = \frac{e^2 q_i q_j}{4\pi\epsilon_0 r_{ij}} + 4\epsilon_{ij}\left[\left(\frac{\sigma_{ij}}{r_{ij}}\right)^{12} - \left(\frac{\sigma_{ij}}{r_{ij}}\right)^{6}\right] \quad (2)$$

where e is the fundamental charge of an electron, q_i and q_j are partial atomic charges and ϵ_0 is the permittivity of vacuum. The Lennard-Jones parameters σ_{ij} and ϵ_{ij} correspond to the zero-crossing distance for the energy and the depth of the potential energy well, respectively. Interaction between hydroxyl atoms are computed with a bonded potential that describes the bond stretch energy by a simple harmonic term:

$$E_{ij}^{\text{bond}} = k_1(r_{ij} - r_0)^2 \tag{3}$$

where k_1 is a force constant and r_0 the equilibrium bond length. Interaction parameters used in this study are provided in Table 1. As there are no parameters for Ar in ClayFF, we assigned it a zero charge and Lennard-Jones parameters as reported by White (1999). The nonbonded parameters are given for interactions between identical atom types ($i = j$). Interaction parameters between unlike atoms ($i \neq j$) are calculated using the Lorentz-Berthelot mixing rules:

$$\sigma_{ij} = \frac{1}{2}(\sigma_i + \sigma_j) \tag{4}$$

$$\epsilon_{ij} = \sqrt{\epsilon_i \epsilon_j} \tag{5}$$

The muscovite atomic model was optimized in a series of preliminary calculations consisting of energy minimization followed by 250 ps MD runs performed in the isobaric-isothermal (NPT) ensemble using the Nosé-Hoover thermostat and barostat, with damping parameters for temperature and pressure of 0.01 and 1 ps, respectively, and a time step of 0.001 ps. Short-range interactions were evaluated with a cut-off distance of 10 Å whereas long-range interactions were treated using the Ewald summation. The ^{40}Ar diffusion energy barriers were quantified using the Nudged Elastic Band (NEB) method (Jónsson et al., 1998), which determines the minimum energy path (MEP) between two stable sites by solving simultaneously independent system images, each one containing one ^{40}Ar atom located on the path connecting the stable sites. Images are linked by a spring force to ensure the continuity of the path and the equal spacing between images along the MEP. The migration energy is obtained by taking the difference in energy between the saddle point and the initial stable site. In this study, eight images were generated and all the NEB calculations were performed with a spring constant of 23 kcal.mol^{-1}.Å^{-2}.

The transport rate based on those migration barriers was evaluated using the Transition State Theory (TST) that expresses the jump probability γ as:

$$\gamma = \nu \exp\left(\frac{-E}{RT}\right) \tag{6}$$

where ν is the attempt frequency, E the migration barrier, R the gas constant, and T the temperature of the system (in Kelvin). The attempt frequency is given by:

$$\nu = \frac{\prod_{i=1}^{3N} \nu_i^{init}}{\prod_{i=1}^{3N-1} \nu_i^{*}} \tag{7}$$

in which ν_i^{init} corresponds to the modal vibrational frequencies at the stable site and ν_i^* represents the non-imaginary modal frequencies at the saddle point (Vineyard, 1957). For most solids, the attempt frequency is comprised between 10^{12} s^{-1} and 10^{13} s^{-1}. This parameter is usually approximated by a fixed value within this interval to avoid the computationally expensive determination of modal frequencies. In this work, we used $\nu = 5 \times 10^{12}$ s^{-1}, which is close to the attempt frequency of 4.61×10^{12} s^{-1} computed via DFT for Ar in lizardite (Wang et al., 2020). The diffusion coefficient is related to the transition rate via:

$$D = ga^2\gamma = ga^2\nu \exp\left(\frac{-E}{RT}\right) \tag{8}$$

where g is a numerical constant depending on the geometry of the lattice and a is the distance between two neighboring stable sites. The frequency factor D_0 is given by:

$$D_0 = ga^2\nu \tag{9}$$

3. Force field validation

To validate the application of the ClayFF force field to the study of muscovite, we compared the lattice parameters computed at ambient conditions (P = 0.001 kbar and T = 25 °C) for our muscovite atomic model with experimental data (Catti et al., 1989). The results (Table 2) show that ClayFF reproduces the experimental crystal structure well. The lattice parameters a, b, c and the angles α, β, γ are all within 2 % (and in most cases 0.5 %)

of the experimental values. The interlayer separation is also well reproduced (within 1 % of experimental determinations). Moreover, ClayFF also faithfully reproduces the stacking of adjacent T−O−T layers. In the interlayer region, the basal oxygens of one T−O−T layer are directly above those of the adjacent layer, in keeping with experimental determinations. Each potassium atom is located at the center of the upper and lower tetrahedral rings. As expected for a di-octahedral mica, the hydroxyl groups point towards the vacant octahedral site and remain subparallel to the (001) plane.

4. ^{40}Ar initial position from interlayer recoil dynamics

The investigation of ^{40}Ar diffusion at the atomic scale requires the determination of its insertion site within the muscovite structure. Since ^{40}Ar is produced with a kinetic energy of 660 kcal.mol^{-1} corresponding to a velocity of 0.11765 Å.fs^{-1} (Dong et al., 1995; Szczerba et al., 2015), the ^{40}Ar insertion site can be determined by modelling the natural ^{40}Ar recoil via MD simulations. Such simulations have been performed by Szczerba et al. (2015), who investigated the natural recoil of ^{40}Ar in illite, a clay mineral structurally similar to muscovite. Using both REAXFF and ClayFF force fields, they performed several simulations in which ^{40}Ar had the same initial velocity (0.11765 Å.fs^{-1}) but varying recoil angles to cover all possible values within a hemisphere. They identified four possible final positions of ^{40}Ar. For recoil vectors subparallel to the (001) plane, ^{40}Ar systematically remained in the interlayer region, occupying either the initial site of the parent ^{40}K or a neighboring vacancy. For recoil vectors pointing towards the T−O−T sheet, ^{40}Ar remained mainly in the interlayer region (79.5 %) but also penetrated into the T−O−T layer (20.5 %), where it ended up either in the tetrahedral layer adjacent to the interlayer region (16.5 %), or in the octahedral layer (1.5 %) or in the opposite tetrahedral layer (2.5 %).

In this work, we simulate the trajectory of the ^{40}Ar recoil in muscovite using the same methodology as Szczerba et al. (2015). Since the penetration of ^{40}Ar into the T−O−T layer induces deformations in the crystal structure (Szczerba et al., 2015), and ClayFF being a non-reactive force field designed to model undeformed structures (Cygan et al., 2004), we investigated recoil trajectories parallel to the interlayer region only. We consider that ^{40}Ar penetrates into the muscovite T−O−T layer in the same proportions as in illite, due to

the similarity of their structures. We define the recoil angle ϕ as the angle between the crystallographic direction a and the recoil vector. The simulations were carried out for recoil angles from 0° to 360° with a step of 20°. In order to simulate a system under geological conditions, we equilibrated first the system in the NPT ensemble, at a temperature of 500 °C and a pressure of 5 kbar. The recoil simulations were then carried out in the NVT ensemble, for a duration of 250 ps with a time step of 1 fs.

The simulations reveal that, in the absence of vacancies in the immediate vicinity of the parent ^{40}K initial site, when the recoil vector is oriented towards a neighboring potassium atom (i.e. for $\phi = 0°$, 60°, 120°, 180° and 240°) the radiogenic ^{40}Ar bounces back from that neighboring K^+ and returns to its initial interlayer position. For the other recoil angles, ^{40}Ar is first propelled into an interstitial position where it remains for about 50 ps, before either returning in its initial position or replacing a neighboring K^+ which is in turn pushed into the ^{40}Ar initial site. Along with Szczerba et al. (2015), this is the first theoretical verification that radiogenic ^{40}Ar initially resides predominantly close to its production site in K−bearing phyllosilicates (Dong et al., 1995), and not many unit cells away as sometimes suggested.

The variation of the total energy of the system when the radiogenic ^{40}Ar is propelled into the interstitial site was computed relative to the mean energy of the system when ^{40}Ar resides in a regular interlayer site. The simulations reveal that when ^{40}Ar is in the interstitial site, i.e., during the first 50 ps, the system has a mean total energy of about 100 kcal.mol^{-1} higher than when ^{40}Ar occupies a regular interlayer site (Fig. 2). This energy increase is due to the distortion that ^{40}Ar causes to the muscovite structure because of its large size. Simulation snapshots (not shown) reveal that when ^{40}Ar is located in the interstitial position, it repeals its neighboring basal oxygens, increasing locally the interlayer spacing by ca. 15 %. This is a highly unfavourable configuration energetically, precluding protracted ^{40}Ar residence in the interstitial site and making unlikely a reincorporation of ^{40}Ar into the interstitial sites once it has lost its initial recoil velocity. This rules out interstitial mechanism as a viable mechanism for ^{40}Ar diffusion in muscovite on geologic timescales.

5. Pathways and ^{40}Ar diffusion barriers in muscovite

The foregoing simulations suggest that the easiest way for ^{40}Ar to move within the muscovite structure without causing major distortions is by jumping into neighboring interlayer vacancies. Vacancies are always present in minerals. They form at high temperature to reduce the Gibbs free energy of the crystal (Mehrer, 2007). Beside those intrinsic vacancies, additional vacancies can be introduced in the mica interlayer region via the pyrophyllitic substitution $\mathrm{Si} + \square \rightarrow {}^{\mathrm{IV}}\mathrm{Al} + \mathrm{K}$ (Tardy and Fritz, 1981; Aagaard and Helgeson, 1983; Helgeson and Aagaard, 1985; Wang and Banno, 1987; Baldelli et al., 1989; Wunder and Melzer, 2002). Their abundance estimated from the commonly measured stochiometric deficit of interlayers cations (up to ca. 10 %) suggests that they can be involved in the motion of interlayer atoms. Therefore, we performed MD simulations in which we initially positioned ^{40}Ar in an interlayer K^+ site and added interlayer vacancies in its vicinity. Simulations were performed in the NPT ensemble at temperatures of 650 to 750 °C and $P = 5$ kbar, for time durations up to 25 ns. No migration could be observed; neither ^{40}Ar nor K^+ atoms jumped into the vacancies. This immobility suggests high migration energy barriers, making diffusion through a vacancy mechanism an infrequent event, unobservable on the timescales of classical MD.

To overcome the timescale limitation, we studied ^{40}Ar diffusion using TST. This requires the migration paths and the migration energies of diffusing atom to be determined first, unlike classical MD simulations which only require initial positions and velocities of atoms. The ^{40}Ar migration energies from its interlayer sites to neighboring vacancies were computed using the NEB method. Since the value of the migration energy in Eqs. (6) and (8) corresponds to the migration barrier of a system at the absolute zero, we first equilibrated the system via NPT simulations at $P = 0$ kbar and $T = -273.1$ °C (i.e., 0.5 K since there is no dynamics at 0 K). The migration of ^{40}Ar in the muscovite interlayer region depends on the presence of a vacancy in its immediate vicinity. Since vacancies can initially form far from the ^{40}Ar site, a motion of potassium atoms along the interlayer region is required for a vacancy to end next to ^{40}Ar so the K^+ migration barriers must be also determined. Furthermore, because vacancies move essentially either individually or by pairs (vacancy clusters involving more than two vacancies being thermodynamically less stable; Mehrer, 2007), we considered the migration barriers for these two configurations, i.e., the migration energies of ^{40}Ar and K^+

from their sites towards a simple vacancy (monovacancy mechanism, labelled "□"; Fig. 3a), or towards a vacancy adjacent to another vacancy (divacancy mechanism, labelled "□□"; Fig. 3b). As the environment around each interlayer site is variable, in particular because of the irregular distribution of Al in the tetrahedral layers, the statistical (probabilistic) calculations must take into account the configuration of atoms in the vicinity of ^{40}Ar and K^+. We positioned thus the ^{40}Ar and K^+ in all the interlayer sites of the model and computed the migrations energies towards all possible neighboring sites. The charge deficit induced by the incorporation of ^{40}Ar and vacancies into the interlayer region was compensated by substituting Al atoms for Si in tetrahedral sites far from the ^{40}Ar migration path (some unit cells away). Our results show that, in the case of the divacancy mechanism, the migration barriers related to the "black" jumps (Fig. 3b) are identical to the energy barriers associated with the monovacancy mechanism. Therefore, we report below 216 migration energies for the monovacancy mechanism (all possible combinations), and 432 for the divacancy mechanism (corresponding only to the "blue" jumps).

5.1. ^{40}Ar migration barriers

The energy barriers associated with the interlayer migration of ^{40}Ar towards neighboring vacancies display wide distributions (Fig. 4a, b). The migration barriers associated with the monovacancy mechanism yield a mean value of 71 ± 5 kcal.mol^{-1} (1σ), while those related to the divacancy mechanism show a slightly lower but statistically indistinguishable mean value of 69 ± 6 kcal.mol^{-1} (1σ). These values are similar to the energy barrier of 69 kcal.mol^{-1} computed using DFT for the migration of Ar in lizardite (Wang et al., 2020), which consists of a stacking of tetrahedral and octahedral layers like muscovite (Mellini, 1982). The similarity between the migration barriers related to both mechanisms is illustrated by the variation of the ^{40}Ar potential energy along its migration path between two neighboring stable sites (corresponding to images "1" and "8"; Fig. 4c). In this example, the energy barrier related to the migration of ^{40}Ar towards a single vacancy is 65 kcal.mol^{-1} while that associated with the jump of ^{40}Ar into a pair of vacancies is 61 kcal.mol^{-1}. In both cases, the forward and backward migration barriers are similar, and this has been observed for all computed paths. The minimum energy paths followed by ^{40}Ar during these jumps (Fig. 4d) reveal that when jumping into a single vacancy, ^{40}Ar follows an almost rectilinear trajectory, passing directly

below the basal oxygens crossed along the path. When it migrates into a pair of vacancies, ^{40}Ar follows a similar trajectory but avoids the basal oxygens, passing quite closer to the vacancy not involved in the migration path. The slight difference in trajectories shows that the difference in magnitude between the respective migration barriers is directly related to the presence or not of a K^+ around the pathway.

The migration barriers are anticorrelated to the total electrostatic energies calculated for each Ar-vacancy configuration in the muscovite model (Fig. 4e). Ruiz Pestana et al. (2017) also report such anticorrelation between the potassium migration energies and the cohesive energies of K^+ at stable sites in illite. These observations suggest that the observed variability in the magnitude of the energy barriers in our model is related to the nonuniform distribution of electrostatic charges around the migration paths, which results from the irregular distribution of Al atoms in the tetrahedral layers. The highest migration barriers are related to paths with less tetrahedral Al around, in contrast to the lowest energies obtained for those surrounded by more tetrahedral Al. In addition to the irregular distribution of tetrahedral Al atoms, variations in the magnitude of migrations barriers also depend to some extent on the relative position of the octahedral vacancies with respect to the migration path. In $2M_1$ muscovite, the projection of octahedral cations and interlayer atoms (K^+) on the (001) plane shows that the octahedral vacancies are located directly above the migration paths forming angles of $\pm$ 60 $^\circ$ and $\pm$ 120 $^\circ$ with the a axis. We observe that for migration paths with the same number of surrounding tetrahedral Al, migration energies are systematically higher for paths parallel to the a axis. These observations suggest a non-negligible effect of the mica structure on the intrinsic diffusion of ^{40}Ar within the interlayer region, as suggested by previous observations and empirical predictions (Scaillet et al., 1992; Dahl, 1996).

5.2. K^+ migration barriers

As with ^{40}Ar, the K^+ migration barriers define wide distributions (Fig. 5a, b). Migrations energies towards monovacancies show a mean value of 79 $\pm$ 9 kcal.mol^{-1} (1σ). Using DFT simulations, Yu et al. (2016) computed energy barriers associated with the migration of K^+ towards a single vacancy in muscovite, for atomic models differing in their number of tetrahedral Al surrounding the interlayer region where the migrating potassium is located. They report energy barriers of (i) 82 kcal.mol^{-1} for the Al−Al model which contains Al

atoms in the two tetrahedral layers adjacent to the interlayer region; (ii) 146 kcal.mol^{-1} for the Al−Si model in which Al atoms are present only in one of the tetrahedral layers, and (iii) 227 kcal.mol^{-1} for the Si−Si model with tetrahedral layer adjacent to the considered interlayer layer region fully occupied by Si atoms. Noteworthy, the energy barrier reported for their Al−Al model, which is equivalent to ours, is within the range of values computed in our study with ClayFF. Ruiz Pestana et al. (2017) report a distribution of K^+ energy barriers in illite computed via ClayFF and DFT. They get mean values of 54 ± 12 kcal.mol^{-1} for ClayFF energy barriers and 75 ± 8 kcal.mol^{-1} for those computed using DFT. They conclude that ClayFF underestimates energy barriers due to the non-bonded nature of the force field which makes structures excessively deformable. However, this apparent discordance between ClayFF and DFT is probably related to the fact that Ruiz Pestana et al. (2017) performed their ClayFF simulations without prior equilibration of their illite structure. In our study, the K^+ energy barriers computed using ClayFF after prior equilibration of the muscovite structure are in the range of their DFT-computed barriers.

The K^+ energy barriers associated with the divacancy mechanism yield a mean value of 66 ± 10 kcal.mol^{-1} (1σ). This value is significantly lower than the mean energy barrier related to the migration of K^+ into a single vacancy. This pronounced difference is illustrated by the variation of the potential energy along the K^+ migration path between two adjacent stable sites (Fig. 5c). In this example, the K^+ energy barrier associated with the monovacancy mechanism is 70 kcal.mol^{-1} and the K^+ energy barrier related to the divacancy mechanism 55 kcal.mol^{-1}. The minimum energy paths followed by K^+ during these migrations show that, in both cases, the potassium atom follows a curvilinear trajectory avoiding the basal oxygen atoms along the path (Fig. 5d). However, in the case of the divacancy mechanism, potassium passes further away from the oxygen atoms than in the monovacancy mechanism. This suggests that the decrease in the migration energy is due to the ability of K^+ ions to minimize interactions with the oxygen atoms lying on their path. Moreover, while ^{40}Ar is at the same energy level in two neighboring vacancies, potassium shows an energy difference between the two sites (Fig. 5c). This is because potassium (charged) is more sensitive to the local charge distribution than ^{40}Ar (neutral). Despite these structural-charge differences, the K^+ and ^{40}Ar energy barriers are positively correlated (Fig. 5e), suggesting a similar influence

of the local environment on the migration energy landscape.

6. ^{40}Ar diffusion coefficients

In this section, we calculate the ^{40}Ar diffusion coefficients in muscovite for both the monovacancy and the divacancy mechanisms by TST (Eq. (8)). Since the investigated migrations occur along the interlayer region, we perform calculations for 2D diffusion in a hexagonal lattice. As given above, Eq. (8) allows the analytical derivation of the diffusion coefficient for a pristine and homogenous crystal, i.e., a crystal in which the migration barrier is the same for all equivalent jumps. In our case, because of the irregular distribution of Al atoms in the tetrahedral layers, the energy barriers of interlayer atoms vary from one direction to another, and from one interlayer site to another. To take into account the spatial variation of the migration barrier, we consider for each diffusing atom an overall effective migration energy, E_{eff}, defined as:

$$\exp\left(\frac{E_{\text{eff}}}{RT}\right) = \sum_{i=1}^{n} \frac{1}{n} \exp\left(\frac{E_i}{RT}\right) \tag{10}$$

where E_i is the effective energy barrier required for an atom to leave an interlayer site i and n is the total number of stable sites in the interlayer region. The effective energy barrier for each site (E_i) is derived from:

$$\exp\left(\frac{-E_i}{RT}\right) = \sum_{j=1}^{m} \frac{1}{m} \exp\left(\frac{-E_{ij}}{RT}\right) \tag{11}$$

in which E_{ij} is the migration energy for leaving the interlayer site i in the direction j, and m is the number of all possible directions ($m = 6$ in a hexagonal lattice).

Eqs (10) and (11) are justified by making an analogy with an electric circuit. When different paths from a given site are possible, the conductances of the paths add up. As the conductance is proportional to the Boltzmann factor, this leads to Eq. (11). A consequence is that the path having the lowest migration energy dominates. When considering a set of sites, they are travelled in sequence so that the resistances add up as expressed by Eq. (10). In particular a site having a high migration energy will slow down the entire diffusion process, this is the trapping effect. Using the energy barriers calculated in section 5, we obtain effective ^{40}Ar migration energy barriers $E_{\text{eff}}^{\text{Ar}\square} = 69$ kcal.mol^{-1} and $E_{\text{eff}}^{\text{Ar}\square\square} = 65$ kcal.mol^{-1} for the

monovacancy and the divacancy mechanism, respectively. For K^+ (or vacancy) migration, the calculated effective barriers are $E_{\text{eff}}^{\text{K}\square} = 75$ kcal.mol^{-1} (monovacancy mechanism) and $E_{\text{eff}}^{\text{K}\square\square} = 58$ kcal.mol^{-1} (divacancy mechanism).

6.1. Monovacancy mechanism

6.1.1. Diffusion of monovacancies in a hexagonal lattice of K^+

The diffusion of ^{40}Ar via the monovacancy mechanism requires the presence of a vacancy in one of its neighboring sites. As long as no vacancies are available, ^{40}Ar cannot move, requiring first to study the diffusivity of the vacancies in the interlayer region. When a vacancy is present in the interlayer region, it is filled by the jump of a neighboring K^+ which, in turn, releases a vacancy in its initial site (Fig. 3a). The displacement vectors have as components:

$$\overrightarrow{V_0} = \begin{pmatrix} \frac{1}{2}a \\ \frac{\sqrt{3}}{2}a \end{pmatrix} \overrightarrow{V_1} = \begin{pmatrix} -\frac{1}{2}a \\ \frac{\sqrt{3}}{2}a \end{pmatrix} \overrightarrow{V_2} = \begin{pmatrix} -a \\ 0 \end{pmatrix} \overrightarrow{V_3} = \begin{pmatrix} -\frac{1}{2}a \\ -\frac{\sqrt{3}}{2}a \end{pmatrix} \overrightarrow{V_4} = \begin{pmatrix} \frac{1}{2}a \\ -\frac{\sqrt{3}}{2}a \end{pmatrix} \overrightarrow{V_5} = \begin{pmatrix} a \\ 0 \end{pmatrix} \quad (12)$$

and the variance of the displacement of the vacancy is:

$$\Delta x^2 = \Delta y^2 = \frac{a^2}{2} \quad (13)$$

We denote by $\gamma_{K_\square}$ the frequency of the jump of one of the neighbouring K^+ towards a monovacancy (noted $K^+ \leftrightarrows \square$), ν the attempt frequency, and $E_{\text{eff}}^{\text{K}\square}$ the migration barrier of K^+. According to TST, the jump frequency is given by:

$$\gamma_{K_\square} = \nu \exp\left(-\frac{E_{\text{eff}}^{\text{K}\square}}{RT}\right) \quad (14)$$

The timelife of the vacancy (i.e., the average time for a successful displacement) is:

$$\Delta t_K = \frac{1}{6\gamma_{K_\square}} \quad (15)$$

and the 2D diffusion coefficient of the vacancy is:

$$D_\square = \frac{\Delta x^2 + \Delta y^2}{4\Delta t_K} = \frac{3}{2}a^2\nu \exp\left(-\frac{E_{\text{eff}}^{\text{K}\square}}{RT}\right) \quad (16)$$

where a is the distance between two neighboring interlayer sites ($a = 5.2$ Å). At $T = 700$ °C, the diffusion coefficient of a single vacancy is $D_\square = 2.88 \times 10^{-19}$ cm^2.s^{-1}.

6.1.2. ^{40}Ar diffusion in a monovacancy flux

Each time a vacancy gets next to a ^{40}Ar atom it is surrounded by five K^+ ions. Interchange between the ^{40}Ar and vacancy positions (noted $^{40}\text{Ar} \leftrightarrows \square$) occurs due to thermal agitation and the lower barrier potential of $^{40}\text{Ar} \leftrightarrows \square$ relative to $K^+ \leftrightarrows \square$. The average duration of these Ar-vacancy oscillations is therefore:

$$\Delta t_{\text{osc}} = \frac{1}{5\gamma_{K_\square}} \tag{17}$$

During this time, many oscillations will have occurred with equal probability 0.5 of ending up either in the initial configuration (no exchange) or in effective migration of ^{40}Ar into the vacancy. The oscillations stop when one of the five K^+ neighbors jumps into the vacancy. For three of these K^+, a successful jump will remove the vacancy away from ^{40}Ar, stopping the $^{40}\text{Ar} \leftrightarrows \square$ oscillations. For the other two, the vacancy stays in the vicinity of ^{40}Ar and the oscillations can resume among the newly created Ar-vacancy pair.

Summing up, when a vacancy gets close to ^{40}Ar, after an average time Δt_{osc}, four different configurations are possible:

- The vacancy has gone away leaving ^{40}Ar in its initial position with a probability of 3/10.
- The vacancy has moved into one of the two neighboring positions of ^{40}Ar with a probability of 2/10. Oscillations resume among the newly-created ^{40}Ar-vacancy pair.
- The $^{40}\text{Ar} \leftrightarrows \square$ interchange is successful and the vacancy moves further away by more than one lattice position with probability of 3/10.
- The $^{40}\text{Ar} \leftrightarrows \square$ interchange has occurred but leaving the vacancy next to ^{40}Ar with probability of 2/10. Oscillations resume again among the new Ar-vacancy pair.

The average number of jumps $\langle n_s \rangle$ needed to move the vacancy away from ^{40}Ar can be calculated by combining the respective probabilities:

$$\langle n_s \rangle = \frac{3}{5}\sum_{n=1}^{\infty} n\left(\frac{2}{5}\right)^{n-1} = \frac{5}{3}\frac{1}{(1-2/5)^2} = \frac{5}{3} \tag{18}$$

According to Eq. (18), the average residence time of the vacancy in the vicinity of ^{40}Ar (the timelife of this configuration) is:

$$\Delta t_o = \frac{5}{3}\Delta t_{\text{osc}} = \frac{1}{3\gamma_{K_\square}} \tag{19}$$

During this time interval, several trains of oscillations will have occured. The calculation of the variance of the mean displacement of ^{40}Ar is complicated by the fact the successive displacements are correlated. However, KMC simulations show that the positional variance of the displacement of $\square$ along either $\overrightarrow{x}$ or $\overrightarrow{y}$ is completely defined by the number of jumps n_s of the vacancy remaining in the neighborhood:

$$\langle \Delta x^2 \rangle = \langle \Delta y^2 \rangle = \frac{n_s + 1}{8} a^2 \tag{20}$$

By summing over the n_s probabilities, we obtain the average variance resulting in the nearest-neighbor vacancy configuration:

$$\langle \Delta x^2 \rangle = \langle \Delta y^2 \rangle \quad = \quad \frac{a^2}{3} \tag{21}$$

Note that, despite its higher energy barrier, the variance is stochastically dominated by the bulk motion of K^+ via the $K^+ \leftrightarrows \square$ interchange (vacancy diffusion), not the mobility of ^{40}Ar with respect to the vacancy. The vibrational motion of ^{40}Ar just ensures that it will take (with probability 0.5) a quantum step away from its initial position when the vacancy passes close by. Note also that this is the variance induced by the proximity of a vacancy. Most of the time, no vacancy hangs around ^{40}Ar which cannot move then (the time goes on with the variance remaining unchanged).

We now inquire into the bulk vacancy flux that governs the overall mobility of ^{40}Ar through the muscovite interlayer. Consider a portion of lattice containing N regular interlayer sites with a single ^{40}Ar atom and a density of vacancies ρ. The number of neighboring sites around a vacancy is six and the number of vacancies $N\rho$. At each vacancy jump, the probability of starting from either a normal "bulk" position or next to ^{40}Ar is proportional to their respective populations. The probability of starting from a neighboring site must be weighted by a factor of 5/6 because only five directions allow it to be reached, instead of six for a normal site. This quantitative reduction has been tested by KMC simulation (Appendix A). Finally, during a vacancy jump the probability of starting from a bulk site is $P_b = (N-6)/N$ while that of jumping from the vicinity of ^{40}Ar is $P_v = 6/N(5/6) = 5/N$.

Consider now a trajectory of m jumps of the $N\rho$ vacancies. Among these m jumps mP_b will start from a bulk site whose lifetime is $t_b = 1/(6\gamma_{K_\square})$ and mP_v will come from

neighboring sites with lifetime $t_v = 1/(5\gamma_{K_\square})$. The total duration of these trajectories of m jumps is therefore:

$$t = m\left(1 - \frac{6}{N}\right)\frac{1}{6\gamma_{K_\square}} + m\frac{5}{N}\frac{1}{5\gamma_{K_\square}} = \frac{m}{6\gamma_{K_\square}} \tag{22}$$

The average number of vacancy jumps ending next to ^{40}Ar is:

$$m_v = m\frac{5}{N}N\rho = 5\rho\, m \tag{23}$$

We have seen that in the direct-neighbor configuration (Fig. 3a), on average 5/3 jumps move the vacancy away from ^{40}Ar (Eq. (18)). The number of such moves in a bulk vacancy flux is:

$$m'_v = 3\rho\, m \tag{24}$$

According to Eq. (21), each of these moves has variance $a^2/3$ so that on average:

$$\langle \Delta x^2 \rangle = \langle \Delta y^2 \rangle = \rho a^2\, m = 6\rho\gamma_{K_\square} a^2\, t \tag{25}$$

The diffusion coefficient for ^{40}Ar is thus:

$$D_{\mathrm{Ar}_\square} = \frac{\langle x^2 \rangle + \langle y^2 \rangle}{4\,t} = 3\,a^2\,\gamma_{K_\square}\,\rho = 3\,a^2\,\nu\,\rho\,\exp\left(-\frac{E_{\mathrm{eff}}^{\mathrm{K}_\square}}{RT}\right) \tag{26}$$

The temperature dependence of this diffusion mechanism is reported in the Arrhenius diagram (Fig. 6). For example, at $T = 700$ °C and $\rho = 0.1$, the diffusion coefficient is $D_{\mathrm{Ar}_\square} = 5.76 \times 10^{-20}$ cm^2.s^{-1}. The diffusion parameters associated with the monovacancy mechanism are $E = 75$ kcal.mol^{-1} and $D_0 = 4 \times 10^{-3}$ cm^2.s^{-1}.

6.2. Divacancy mechanism

6.2.1. Diffusion of divacancies in a hexagonal lattice of K^+

In the case of a divacancy mechanism, K^+ atoms are adjacent either to only one vacancy or both (Fig. 3b). In the latter configuration, the jumps (blue arrows) have a lower effective energy barrier (58 kcal.mol^{-1}) and therefore a higher probability of occurrence than those of the first configuration (in black), whose migration barriers are identical to those associated with the monovacancy mechanism (75 kcal.mol^{-1}). When one of these "blue" migrations occurs, a K^+ atom fills one vacancy and a new vacancy is created in its initial position. This new vacancy lies in one of the sites neighboring the unoccupied vacancy of the initial

pair, and both form a new vacancy pair. Therefore, one can expect a correlated mobility of divacancies along the interlayer region.

The two pertinent quantities to calculate here are the diffusion coefficient of the divacancy and its lifetime. The divacancy is characterized by its position (barycenter of the vacancy pair), the direction passing through the vacancy pair, and the angle made by the direction with the x-axis which can be 0° (Fig. 3b) or ± 60°. Each atom jump filling a vacancy produces a virtual displacement and the apparent rotation of the divacancy direction. Let us calculate the average variance of such a displacement.

When the starting angle is 0° the jumps $\overrightarrow{\delta_0}$, $\overrightarrow{\delta_1}$, $\overrightarrow{\delta_2}$, $\overrightarrow{\delta_3}$ produce respectively the angles 60°, 60°, −60°, −60°, and the divacancy displacement vectors:

$$\overrightarrow{V_0} = \begin{pmatrix} \frac{1}{4}a \\ \frac{\sqrt{3}}{4}a \end{pmatrix} \qquad \overrightarrow{V_1} = \begin{pmatrix} -\frac{1}{4}a \\ -\frac{\sqrt{3}}{4}a \end{pmatrix} \qquad \overrightarrow{V_2} = \begin{pmatrix} \frac{1}{4}a \\ -\frac{\sqrt{3}}{4}a \end{pmatrix} \qquad \overrightarrow{V_3} = \begin{pmatrix} -\frac{1}{4}a \\ \frac{\sqrt{3}}{4}a \end{pmatrix} \tag{27}$$

By symmetry, these jumps are equiprobable.

For a starting angle of 60°, the divacancy displacement vectors $\overrightarrow{V_i}$ are just rotated by this angle :

$$\overrightarrow{V_i}' = \begin{pmatrix} \frac{1}{2} & -\frac{\sqrt{3}}{2} \\ \frac{\sqrt{3}}{2} & \frac{1}{2} \end{pmatrix} \overrightarrow{V_i} \tag{28}$$

and:

$$\overrightarrow{V_0}' = \begin{pmatrix} -\frac{1}{4}a \\ \frac{\sqrt{3}}{4}a \end{pmatrix} \qquad \overrightarrow{V_1}' = \begin{pmatrix} \frac{1}{4}a \\ -\frac{\sqrt{3}}{4}a \end{pmatrix} \qquad \overrightarrow{V_2}' = \begin{pmatrix} \frac{1}{2}a \\ 0 \end{pmatrix} \qquad \overrightarrow{V_3}' = \begin{pmatrix} -\frac{1}{2}a \\ 0 \end{pmatrix} \tag{29}$$

For the −60° configuration, the corresponding rotation is:

$$\overrightarrow{V_0}'' = \begin{pmatrix} \frac{1}{2}a \\ 0 \end{pmatrix} \qquad \overrightarrow{V_1}'' = \begin{pmatrix} -\frac{1}{2}a \\ 0 \end{pmatrix} \qquad \overrightarrow{V_2}'' = \begin{pmatrix} -\frac{1}{4}a \\ -\frac{\sqrt{3}}{4}a \end{pmatrix} \qquad \overrightarrow{V_3}'' = \begin{pmatrix} \frac{1}{4}a \\ \frac{\sqrt{3}}{4}a \end{pmatrix} \tag{30}$$

Whatever the starting configuration, it can be shown that $\langle x \rangle = \langle x \rangle = 0$. For a given trajectory, the orientations are equiprobable. For all jumps keeping the vacancy pair connected the displacements $\overrightarrow{V_i}, \overrightarrow{V_i}'$ and $\overrightarrow{V_i}''$ occur with equal probability of 1/12. One may verify that $\langle x \cdot y \rangle = 0$, indicating that the displacements along either x or y are uncorrelated which is a consequence of hexagonal symmetry. In terms of variance of displacements we have:

$$\langle x^2 \rangle = \langle y^2 \rangle = \frac{1}{8}a^2 \tag{31}$$

due again to the symmetry in x and y.

Denote by $\gamma_{K_\square}$ the jump frequency corresponding to a "black" migration and $\gamma_{K_{\square\square}}$ for the "blue" migration (Fig. 3b). The residence time of the divacancy at any given position is:

$$t_r = \frac{1}{4\gamma_{K_{\square\square}} + 6\gamma_{K_\square}} \tag{32}$$

The average migration time after m jumps is:

$$\langle t \rangle = m\, t_r = \frac{m}{4\gamma_{K_{\square\square}} + 6\gamma_{K_\square}} \tag{33}$$

and the variance of the displacement:

$$\langle x^2 \rangle = \langle y^2 \rangle = m\frac{a^2}{8} \tag{34}$$

From these, we deduce the divacancy diffusion coefficient:

$$D_{\square\square} = \frac{1}{4}a^2\left(\gamma_{K_{\square\square}} + \frac{3}{2}\gamma_{K_\square}\right)$$

$$D_{\square\square} = \frac{1}{4}a^2\nu\exp\left(-\frac{E_{\text{eff}}^{\text{K}\square\square}}{RT}\right)\left[1 + \frac{3}{2}\exp\left(\frac{E_{\text{eff}}^{\text{K}\square\square} - E_{\text{eff}}^{\text{K}\square}}{RT}\right)\right] \tag{35}$$

where $E_{\text{eff}}^{\text{K}\square\square}$ is the K^+ migration barrier towards a divacancy. The second exponential in parentheses (rightmost term) is much smaller than unity and the diffusion coefficient reduces to:

$$D_{\square\square} = \frac{1}{4}a^2\nu\exp\left(-\frac{E_{\text{eff}}^{\text{K}\square\square}}{RT}\right) \tag{36}$$

At $T = 700$ °C, the diffusion coefficient associated with the divacancy migration is $D_{\square\square} = 3.89 \times 10^{-16}$ cm^2.s^{-1}, three orders of magnitude faster than the monovacancy mechanism.

6.2.2. ^{40}Ar diffusion in a divacancy flux

When a divacancy lies in the vicinity of ^{40}Ar, the latter can be adjacent to either one or both vacancies and the probability that one is filled by ^{40}Ar depends on the specific nearest-neighbor configuration. Denote by $E_{\text{eff}}^{\text{Ar}\square}$ the ^{40}Ar energy barrier faced by the "black" transitions and by $E_{\text{eff}}^{\text{Ar}\square\square}$ that associated with "blue" migrations. When the ^{40}Ar is adjacent to only one of the two vacancies (Fig. 3b) the probability of jump before a move of the

divacancy is:

$$P_{\mathrm{Ar}_{\square}} = \frac{\exp\left(-\frac{E_{\mathrm{eff}}^{\mathrm{Ar}_{\square}}}{RT}\right)}{\exp\left(-\frac{E_{\mathrm{eff}}^{\mathrm{Ar}_{\square}}}{RT}\right) + 5\exp\left(-\frac{E_{\mathrm{eff}}^{\mathrm{K}_{\square}}}{RT}\right) + 2\exp\left(-\frac{E_{\mathrm{eff}}^{\mathrm{K}_{\square\square}}}{RT}\right)}$$

$$= \frac{\exp\left(-\frac{E_{\mathrm{eff}}^{\mathrm{Ar}_{\square}} - E_{\mathrm{eff}}^{\mathrm{K}_{\square\square}}}{RT}\right)}{\exp\left(-\frac{E_{\mathrm{eff}}^{\mathrm{Ar}_{\square}} - E_{\mathrm{eff}}^{\mathrm{K}_{\square\square}}}{RT}\right) + 5\exp\left(-\frac{E_{\mathrm{eff}}^{\mathrm{K}_{\square}} - E_{\mathrm{eff}}^{\mathrm{K}_{\square\square}}}{RT}\right) + 2} \tag{37}$$

The exponentials in the denominator are much smaller than one because of the difference in the energy barriers, and Eq. (37) simplifies to

$$P_{\mathrm{Ar}_{\square}} = \frac{1}{2}\exp\left(-\frac{E_{\mathrm{eff}}^{\mathrm{Ar}_{\square}} - E_{\mathrm{eff}}^{\mathrm{K}_{\square\square}}}{RT}\right) \tag{38}$$

On the other hand, there are two positions where the ^{40}Ar is close to both vacancies (Fig. 3b) and the probability of jumping into one of them before the divacancy move is:

$$P_{\mathrm{Ar}_{\square\square}} = \frac{\exp\left(-\frac{E_{\mathrm{eff}}^{\mathrm{Ar}_{\square\square}}}{RT}\right)}{\exp\left(-\frac{E_{\mathrm{eff}}^{\mathrm{Ar}_{\square}}}{RT}\right) + 6\exp\left(-\frac{E_{\mathrm{eff}}^{\mathrm{K}_{\square}}}{RT}\right) + \exp\left(-\frac{E_{\mathrm{eff}}^{\mathrm{K}_{\square\square}}}{RT}\right)} \tag{39}$$

As before, Eq. (39) simplifies to

$$P_{\mathrm{Ar}_{\square\square}} = \exp\left(-\frac{E_{\mathrm{eff}}^{\mathrm{Ar}_{\square\square}} - E_{\mathrm{eff}}^{\mathrm{K}_{\square\square}}}{RT}\right) \tag{40}$$

The relative importance of the probabilities Eqs. (38) and (40) depends on the frequency of each configuration.

Denote by ρ' the density of divacancies in the interlayer region, defined as the number of divacancies divided by the number of interlayer sites in the lattice. Consider a trajectory of m jumps of the divacancies. For $6m\rho'$ positions the ^{40}Ar will be close to one only vacancy, and for $m\rho'$ it will be close to both vacancies. The above expressions can be deduced by weighing the different orientations and by observing that the double-vicinity of the ^{40}Ar can

be reached only from one side, and they have been confirmed by running dedicated KMC simulations (Appendix A.).

In the bulk divacancy flux, the residence time of a divacancy is given by Eq. (32) in which $\gamma_{K_\square}$ can be neglected. This residence time is nearly the same when a ^{40}Ar is close to only one vacancy, but it doubles when it neighbors the two vacancies. Therefore the time for a trajectory of m jumps is:

$$t = \frac{m}{4\gamma_{K_{\square\square}}}(1+\rho') = \frac{m}{4\nu}(1+\rho')\exp\left(\frac{E_{\text{eff}}^{\text{K}_{\square\square}}}{RT}\right) \tag{41}$$

For $6m\rho'$ configurations, ^{40}Ar sees only one vacancy and the jump probability is given by Eq. (38). For $m\rho'$ configurations it neighbors the two vacancies and has a jump probability given by Eq. (40). For any jump the variance in coordinates is given by Eq. (13). In the end, for m jumps the variance is:

$$\langle x^2\rangle = \langle y^2\rangle = m\rho'\frac{a^2}{2}\left[3\exp\left(-\frac{E_{\text{eff}}^{\text{Ar}_\square}-E_{\text{eff}}^{\text{K}_{\square\square}}}{RT}\right)+\exp\left(-\frac{E_{\text{eff}}^{\text{Ar}_{\square\square}}-E_{\text{eff}}^{\text{K}_{\square\square}}}{RT}\right)\right] \tag{42}$$

From Eq. (41) and (42) we can deduce the diffusion coefficient for ^{40}Ar:

$$D_{\text{Ar}_{\square\square}} = \frac{\rho'}{1+\rho'}a^2\nu\left[3\exp\left(-\frac{E_{\text{eff}}^{\text{Ar}_\square}}{RT}\right)+\exp\left(-\frac{E_{\text{eff}}^{\text{Ar}_{\square\square}}}{RT}\right)\right] \tag{43}$$

in which the first term inside the brackets is small compared to the last one.

It remains to determine the density of divacancies ρ'. It can be expressed with the density of monovacancies ρ. The divacancies are produced when two monovacancies hit each other, because their coherent motion is energetically favored. On the other hand they decay when one of its vacancies is filled by a neighboring K^+ (black jumps; Fig. 3). This is a dynamical equilibrium reached when the rate of production equates the rate of decay.

Consider N regular interlayer sites. The number of monocancies is $N\rho$. At any jump of a vacancy, the probability to make a collision (i.e. to reach the neighborhood of another vacancy) is proportional to ρ, so that the number of produced divacancies is $kN\rho^2$, where k is a number to be determined. A dedicated random walk simulation shows that $k = 2.5$. The duration of each step is $1/(6\gamma_{K_\square})$ giving a production rate of $15N\rho^2\gamma_{K_\square}$. The decay rate is $6N\rho'\gamma_{K_\square}$. By equating the two rates one gets $\rho' = 2.5\rho^2$.

After replacement of this value in Eq. (43) and taking into account that $\rho \ll 1$:

$$D_{\mathrm{Ar}_{\square\square}} = \frac{5}{2}\rho^2 a^2 \nu \left[3\exp\left(-\frac{E_{\mathrm{eff}}^{\mathrm{Ar}_{\square}}}{RT} \right) + \exp\left(-\frac{E_{\mathrm{eff}}^{\mathrm{Ar}_{\square\square}}}{RT} \right) \right] \quad (44)$$

At $T = 700$ °C and for $\rho = 0.1$, the ^{40}Ar diffusion coefficient associated with the divacancy mechanism is $D_{\mathrm{Ar}_{\square\square}} = 1.16 \times 10^{-18}$ cm^2.s^{-1}, two orders of magnitude higher than the diffusivity of the monovacancy mechanism. The ^{40}Ar diffusion parameters deduced from the Arrhenius diagram (Fig. 6) are $E = 66$ kcal.mol^{-1} and $D_0 = 6 \times 10^{-4}$ cm^2.s^{-1}. A summary listing of the final estimates is provided in Table 3.

7. Discussion

7.1. Comparison with previous ^{40}Ar diffusion estimates

As mentioned above, only a handful of studies have attempted to quantify ^{40}Ar diffusion in muscovite (Robbins, 1972; Hames and Bowring, 1994; Kirschner et al., 1996; Lister and Baldwin, 1996, 2016; Harrison et al., 2009; Forster and Lister, 2014). While ^{40}Ar diffusivity estimates inferred by these studies are broadly consistent, they considerably differ from the present results. Our MD and TST estimates are up to five orders of magnitude lower than the corresponding Arrhenian laws (Fig. 6). Note that our results are calculated for muscovite at $P = 0$ kbar. Assuming a pressure effect on diffusivity of ^{40}Ar in muscovite (Harrison et al., 2009) would enhance the disparity even further.

Hydrothermal experiments have been suspected to overestimate ^{40}Ar diffusivity in natural muscovite for quite a while now (Monié, 1990; Scaillet et al., 1990, 1992; Monié and Chopin, 1991; Arnaud and Kelley, 1995; Scaillet, 1996; Di Vincenzo et al., 2001, 2004, 2006; Balogh and Dunkl, 2005; Hames et al., 2008; Itaya et al., 2009; Allaz et al., 2011; Beltrando et al., 2013; Halama et al., 2014; Schertl and Hammerschmidt, 2016; Laurent et al., 2021). As emphasized before, most of these studies relate to high-pressure (phengitic) muscovite. The high retentivity (i.e., low ^{40}Ar diffusivity) of muscovite in these conditions has long been traced to crystal-structural effects suspected to affect the interlayer at increasingly higher pressure (Scaillet et al., 1992; Scaillet, 1998). It is also supported by the diffusion data of Harrison et al. (2009) which predict lower diffusivities at high pressure. Evidence for a pronounced ^{40}Ar retentivity in muscovite has been also reported in other settings as well

(e.g. Di Vincenzo et al., 2004; Hames et al., 2008; Itaya et al., 2009; Allaz et al., 2011), suggesting that sluggish ^{40}Ar kinetics in natural muscovite is more the norm than currently acknowledged by existing experimental data.

Field-based calibration of ^{40}Ar retention kinetics in muscovite is scarce and highly context-specific (e.g., Wijbrans and McDougall, 1986, 1988; Blanckenburg et al., 1989; Kirschner et al., 1996). So far, such efforts have been taken to indicate moderate or intermediate ^{40}Ar retention properties of muscovite relative to other isotope-mineral pairs (by order of decreasing retentivity: U/Pb−zircon > Rb/Sr−muscovite > K/Ar−amphibole > K/Ar−muscovite > K/Ar−biotite ≈ K/Ar−alkali feldspar). Mounting evidence, in particular from grain-scale Rb/Sr and laser-based ^{40}Ar/^{39}Ar disequilibrium data (e.g. Bröcker et al., 2013; Cliff et al., 2017; Laurent et al., 2021), shows that Ar-Rb-Sr retention systematics in natural muscovite are actually quite similar (Glodny et al., 2002; 2008; Bosse et al., 2005; Scibiorski et al., 2021), pointing to otherwise more sluggish kinetics than suggested by the above trend for elements that are either ionically bonded (Rb, Sr) and/or simply too big (Ar) to easily jump from a lattice position to the next. This is most clearly illustrated by peak-metamorphic ^{40}Ar/^{39}Ar retention ages commonly preserved in muscovite despite deformation and overprinting (Putlitz et al., 2005; Beaudoin et al., 2020, Laurent et al., 2021). This is also emphasized by congruent ^{40}Ar/^{39}Ar muscovite and U/Pb titanite ages metastably preserved over map-scales in excess of 450-750 km^2 in dry granulite-amphibolite crust exposed to $T \geqslant$ 700 °C for tens of Myr (Spencer et al., 2013).

Using the diffusion data retrieved from our modeling (E = 66 kcal.mol^{-1} and D_0 = 6 × 10^{-4} cm^2.s^{-1}), nominal closure temperatures can be calculated via Eq. (1) for various cooling rates and grain sizes. For cooling rates ranging from 1 to 100 °C.Ma^{-1} and grain size varying between 0.1-1.0 mm, this returns closure temperatures in the range 560-800 °C (Fig. 7). These are significantly (up to 200 °C) higher than predicted by current experimental estimates (Hames and Bowring, 1994; Kirschner et al., 1996; Harrison et al., 2009) and close to the upper stability limit of muscovite (∼ 700 °C; Massonne and Schreyer, 1987, 1989), which by the way is significantly lower in presence of quartz (Althaus et al., 1970). This opens up the prospect that crystallization ages may be more likely than cooling ages in natural muscovite.

However, empirical evidence also abounds to suggest that intracrystalline ^{40}Ar mobility may be enhanced by other factors beyond purely diffusion-driven rates such as predicted by our model. Our model calculations apply to ideal (undefective) muscovite. Natural micas are far from perfect and always contain microstructural defects such as dislocations, stacking faults, microcleavages, etc., which can develop during crystal growth, or more commonly, in response to deformation (e.g. Bell and Wilson, 1977, 1981; Amouric, 1987; Kronenberg et al., 1990; Shea and Kronenberg, 1992; Dunlap, 1997; Beaudoin et al., 2020). Such extended microstructural defects act as high diffusivity pathways that can considerably enhance the mobility of diffusing atoms (Lee, 1995). Sizeable extents of ^{40}Ar loss have been documented in naturally and experimentally deformed muscovite in connection with microstructural defects (Kramar et al., 2001, 2003; Mulch et al., 2002; Cosca et al., 2011). Ascribing the observed losses in such cases to diffusion only is bound to overestimate ^{40}Ar diffusion rates, but to a largely unknown extent if the crystal-defective structure of the mica is not properly quantified (Kramar et al., 2001, 2003). A case in point are the diffusion rates empirically derived from the muscovites studied by Kirschner et al. (1996). These crystallized during deformation by thrusting and most likely contain microstructural defects as well.

The same caveat applies to diffusion experiments performed under hydrothermal conditions (Dunlap, 1997). To optimize the fractional loss of their starting material, Harrison et al. (2009) used fine-grained muscovite fractions (< 100 μm across) obtained by mechanical grinding of larger grains. Such grinding is likely to have produced extended intracrystalline defects in their samples, a problem already raised by Dunlap (1997) for the early thermal-hydrothermal experiments conducted by Robbins (1972). While these defects may have little effect on the effective loss of ^{40}Ar in vacuum (< 0.5 %; Dunlap and Kronenberg, 2001), their impact under hydrothermal conditions may be vastly underestimated because of the longer duration of these experiments. Incidentally, Harrison et al. (2009) used a multi-domain diffusion model in an attempt to fit their hydrothermal-loss data to complex *in vacuo* generated ^{40}Ar/^{39}Ar spectrum patterns. Such a non-ideal behavior may to some extent reflect the complex defective structure artificially induced during sample preparation.

An additional complication is the presence of reactive fluids, both in Nature and experiments. When out of equilibrium with the solid phase, fluid-phase dissolution-precipitation

may lead to partial destabilization depending on fluid-solid equilibria, crystal boundary structure and width, and exchange duration (Cole and Chakraborty, 2001; Putnis, 2009). Fluid-phase dissolution kinetics are much faster than solid-state intracrystalline diffusion (Scaillet, 1998; Putnis, 2009), potentially enhancing ^{40}Ar loss well beyond lattice diffusion rates in hydrothermal experiments. Harrison et al. (2009) report a fractional loss 10 % higher for a hydrothermal run compared to the same $P-T$ run under dry conditions. Although the authors infer that a fluid phase is a necessary reservoir for ^{40}Ar to be diffusively lost from muscovite during the experiments, the difference may also reflect ^{40}Ar diffusion enhanced in the presence of water. Harrison et al. (2009) also report an Al enrichment of their run products compared to the starting material. As discussed by Villa (2021), this may hint at dissolution−precipitation transformations during the runs, potentially compromising (i.e., overestimating) the diffusion rates derived from the observed losses. Evidence of recrystallization of micas during hydrothermal experiments is also reported by Hess et al. (1987) and Villa and Puxeddu (1994).

Although not dealing with ^{40}Ar diffusion in muscovite proper, studies of Sr diffusion in biotite (Hammouda and Cherniak, 2000) have revealed four orders magnitude difference in diffusion rates between hydrothermally treated biotite (faster-diffusing) and dry F-phlogopite (slower-diffusing). These authors rule out F-substitutional effects in favor of the weakening effect of water on the mica structure to explain this behavior, possibly enhanced by dissolution−recrystallization processes during the hydrothermal treatment. Water molecules can also act as source of H^+, which weaken Si−O and Al−O bonds and consequently enhance the diffusion of oxygen in minerals such as quartz (Elphick and Graham, 1988), alkali feldspar (Farver and Yund, 1990) and micas (Fortier and Giletti, 1991). Hydrolysis of K−O bonds in muscovite, similar to that of Si−O and Al−O in other common silicates, could lower the ^{40}Ar migration barrier, thereby accelerating its diffusion. All these mechanisms suggests that ^{40}Ar diffusivity measured under hydrothermal conditions provides only an upper limit to actual ^{40}Ar transport rates across the mica lattice.

7.2. Applicability to natural systems and implications for $^{40}Ar/^{39}Ar$ thermochronology

All the above processes work the same in Nature, but with even more free thermodynamic variables (e.g., multiphase equilibria, transient fluids) and much longer durations than in hy-

drothermal diffusion cells. In fluid-assisted metamorphic transformations, the ^{40}Ar initially present in recrystallized (or dissolved) muscovite may be released in the free fluid phase, locally enhancing or disrupting ^{40}Ar concentration gradients pre-existing in the original crystals (e.g. Hames and Cheney, 1997; Scaillet, 1998; Di Vincenzo et al., 2001, 2004; Hames et al., 2008; Beltrando et al., 2013; Beaudoin et al., 2020; Laurent et al., 2021). Partial to complete ^{40}Ar resetting with intracrystalline ^{40}Ar/^{39}Ar gradients do exist however, as documented *in situ* in natural muscovite (e.g., Scaillet et al., 1990, 1992; Hames and Hodges, 1993; Hodges et al., 1994; Hodges and Bowring, 1995; Scaillet, 1996; Boundy et al., 1997). The mere existence of these spatial gradients is indication that bulk (volume) diffusive motion is effectively operating in Nature, but not with the rate constants and barrier potentials theoretically predicted for ideal (undefective) muscovite. The empirical Ar-Rb-Sr parallel drawn above and the highly disparate ^{40}Ar diffusion rates documented both experimentally and in the field clearly indicate that ^{40}Ar/^{39}Ar systematics in natural systems are not fully captured yet in terms of lattice-scale processes.

Our findings point to a fundamental, yet largely unexplored, crystal-structural thread connecting the Ar isotopic record with mixed-scale diffusional ± compositional ± structural *disequilibrium interactions* during the natural "growth → closure" cycle of muscovite. During metamorphic $P-T$ changes, white micas react via segregation and re-organization of Si^{4+}−rich domains involving the cooperative interdiffusion of several components such as $2Na^{+} + Al^{3+} = K^{+} + Si^{4+} + \square$ that progressively produce discrete compositional domains during re-equilibration (Shau et al., 1991), analogous to segregation of interlayer cations (Na^{+}, Ca^{2+}, K^{+}) into nanodomains (Livi et al., 2008; Beltrando et al., 2013). Crystal-structural evidence above suggests that such modifications are decoupled kinetically across the interlayer hosting radiogenic ^{40}Ar, especially in the presence of grain-scale chemical potential and stress gradients (Scaillet et al., 1992; Scaillet, 1996, 1998), severely impairing the interpretation of microscale ^{40}Ar/^{39}Ar patterns in terms of either diffusion or (re)crystallization (Beaudoin et al., 2020; Laurent et al., 2021).

Hence, the reason why empirical ^{40}Ar diffusion rates are so distinct from DFT and MD estimates is not failure of these approaches in describing fundamental lattice-based processes. Rather, it is the manifestation of atomic-scale kinetics combining diffusion with (as yet)

largely unmodeled physics, most notably those controlling reactivity of the interlayer with the external medium. Thermodynamic equilibrium is the common-denominator assumption of both experimental and theoretical diffusion modeling. So far, fulfilling this condition has proven elusive in the hydrothermal treatment of muscovite (Villa, 2021). In contrast, equilibrium is a built-in condition in theoretical models ensuring, as here, full control on boundary conditions along with a test that the system indeed remains thermodynamically stable. As such, our MD and TST diffusion estimates provide the first reliable benchmark against which to gauge first-order ^{40}Ar diffusion kinetics in a stoichiometrically stable muscovite structure. Combined with hydrothermal predictions (Fig. 6), they collectively define the probable $D-T$ space spanned by intracrystalline ^{40}Ar kinetics in natural muscovite. Further empirical and theoretical work is required to clarify kinetic interactions between crystal-chemical disequilibrium and effective ^{40}Ar diffusion across such $D-T$ space.

8. Conclusions

A lattice-based study of ^{40}Ar diffusion in muscovite has been attempted for the first time via Molecular Dynamics simulations coupled with Nudged Elastic Band and Transition State Theory. The main results lead to the following conclusions:

- ^{40}Ar diffusion in $2M_1$ muscovite predominantly occurs along the (001) interlayer with recoil energies too low to permit extensive or systematic implantation of the radiogenic ^{40}Ar atom more than a lattice spacing away from its production site from ^{40}K.

- Systematic energy-barrier mapping by NEB coupled with TST allows to identify the most probable diffusion pathway and barrier potential for ^{40}Ar motion along the (001) interlayer; ^{40}Ar transport via a divacancy mechanism is shown to be the more energetically favorable pathway for ^{40}Ar migration along (001) with characteristic diffusion parameters $E = 66$ kcal.mol^{-1} and $D_0 = 6 \times 10^{-4}$ cm^2.s^{-1}.

- These theoretical estimates suggest that purely diffusion-driven (Brownian) motion is not an efficient mechanism for ^{40}Ar intracrystalline transport in a stoichiometrically pure and

stable muscovite structure.

• Along with hydrothermal and field-based evidence, they call for more complex (multi-scale and multi-process) physics to explain ^{40}Ar exchange and retention properties of natural muscovite, most notably by considering the chemical-stoichiometric reactivity of the interlayer with the external medium.

Acknowledgements

Work supported by LABEX grant VOLTAIRE (ANR-10-LABX-100-01), the Région Centre grant ARGON, and the EQUIPEX grant PLANEX (ANR-11-EQPX-0036). J. Nteme is supported by a post-doctoral grant from the project LABEX-VOLTAIRE. Jan Wijbrans (VU, Amsterdam) and two anonymous reviewers are thanked for providing insightful comments and references that helped to improve the content and clarity of the work. Associate editor F. Jourdan is thanked for efficient handling of the manuscript as well as for a flash review. Parts of the material and ideas developed in this paper form the basis of the project "DeconvAr" discarded as "unlikely to lead to a breakthrough and widespread application of the findings" under the 2021 AAPG call "Planétologie, structure et histoire de la Terre".

Appendix A. Supplementary Material

Supplementary data associated with this article can be found, in the online version, at http://dx.doi.org/xx.xxx/xxxxxxxxxxxx.

References

Aagaard P. and Helgeson H. C. (1983) Activity/composition relations among silicates and aqueous solutions: II. Chemical and thermodynamic consequences of ideal mixing of atoms on homological sites in montmorillonites, illites, and mixed-layer clays. *Clays and Clay Miner.* **31**, 207-217.

Allaz, J., Engi, M., Berger, A. and Villa I. M. (2011) The effects of retrograde reactions and of diffusion on ^{40}Ar-^{39}Ar ages of micas. *J. Petrol.*, **52**, 691-716.

Althaus E., Karotke E., Nitsch K. and Winkler H. (1970) An experimental re-examination of the upper stability limit of muscovite plus quartz. *Neues Jahrb Miner. Monatsh* **7**, 325–336.

Amouric M. (1987) Growth and deformation defects in phyllosilicates as seen by HRTEM. *Acta Crystal. B* **43**, 57-63.

Argyris D., Ho T., Cole D. R. and Striolo A. (2011a) Molecular dynamics studies of interfacial water at the alumina surface. *J. Phys. Chem. C* **15**, 2038-2046.

Argyris D., Ashby P. D. and Striolo A. (2011b) Structure and orientation of interfacial water determine atomic force microscopy results: insights from molecular dynamics simulations. *ACS nano* **5**, 2215-2223.

Armstrong R. L. (1966) K-Ar dating of plutonic and volcanic rocks in orogenic belts. In *Potassium Argon dating* (eds. O.A. Schaeffer and J. Zähringer). Springer-Verlag, Berlin, p 117-133.

Arnaud N. and Kelley S. P. (1995) Evidence for excess argon during high pressure metamorphism in the Dora Maira Massif (western Alps, Italy), using an ultra-violet laser ablation microprobe ^{40}Ar–^{39}Ar technique. *Contrib. Miner. Petrol.* **121**, 1-11.

Bailey S. W. (1984) Classification and structures of the Micas. In *Micas* (ed. S.W. Bailey). Rev. Miner. **13**, 1-12.

Baldelli C., Franceschelli M., Leoni L. and Memmi I. (1989) Ferrimuscovite and celadonite substitutions in muscovite from Fe^{3+}-rich low-grade psammitic rocks (Northern Apennines, Italy).

Lithos **23**, 201-208.

Balogh K. and Dunkl I. (2005) Argon and fission track dating of Alpine metamorphism and basement exhumation in the Sopron Mts.(Eastern Alps, Hungary): thermochronology or mineral growth? *Miner. Petrol.* **83**, 191-218.

Balout H., Roques J., Gautheron C., Tassan-Got L. and Mbongo-Djimbi D. (2017a) Helium diffusion in pure hematite (α-Fe_2O_3) for thermochronometric applications: A theoretical multi-scale study. *Comput. Theor. Chem.* **1099**, 21-28.

Balout H., Roques J., Gautheron C. and Tassan-Got L. (2017b) Computational investigation of interstitial neon diffusion in pure hematite. *Comput. Mater. Sci.* **128**, 67-74.

Bassal F., Roques J. and Gautheron C. (2020) Neon diffusion in goethite, α-FeO(OH): a theoretical multi-scale study. *Phys. Chem. Miner.* **47**, 1-14.

Beaudoin A., Scaillet S., Mora N., Jolivet L. and Augier R. (2020) In Situ and Step-Heating $^{40}Ar/^{39}Ar$ Dating of White Mica in Low-Temperature Shear Zones (Tenda Massif, Alpine Corsica, France). *Tectonics* **39**, e2020TC006246.

Bell I. A. and Wilson C. (1977) Growth defects in metamorphic biotite. *Phys. Chem. Miner.* **2**, 153-169.

Bell I. A. and Wilson C. (1981) Deformation of biotite and muscovite: TEM microstructure and deformation model. *Tectonophysics* **78**, 201-228.

Beltrando M., Di Vincenzo G. and Ferraris C. (2013) Preservation of sub-microscopic structural relicts in micas from the Gran Paradiso Massif (Western Alps): Implications for ^{40}Ar–^{39}Ar geochronology. *Geochim. Cosmochim. Acta* **119**, 359-380.

Bengtson A., Ewing R. C. and Becker U. (2012) He diffusion and closure temperatures in apatite and zircon: A density functional theory investigation. *Geochim. Cosmochim. Acta* **86**, 228-238.

Blanckenburg F. v., Villa I., Baur H., Morteani G. and Steiger R. (1989) Time calibration of a PT-path from the Western Tauern Window, Eastern Alps: the problem of closure temperatures.

Contrib. Miner. Petrol. **101**, 1-11.

Bosse V., Féraud G., Ballèvre M., Peucat J. J. and Corsini M. (2005) Rb-Sr and $^{40}Ar/^{39}Ar$ ages in blueschists from the Ile de Groix (Armorican Massif, France): Implications for closure mechanisms in isotopic systems. *Chem. Geol.* **220**, 21-45.

Boundy T. M., Hall C. M., Li G., Essene E. J. and Halliday A. (1997) Fine-scale isotopic heterogeneities and fluids in the deep crust: a $^{40}Ar/^{39}Ar$ laser ablation and TEM study of muscovites from a granulite-eclogite transition zone. *Earth Planet. Sci. Lett.* **148**, 223-242.

Bröcker M., Baldwin S. and Arkudas R. (2013) The geological significance of $^{40}Ar/^{39}Ar$ and Rb–Sr white mica ages from Syros and Sifnos, Greece: a record of continuous (re)crystallization during exhumation? *J. Metam. Geol.* **31**, 629-646.

Catti M., Ferraris G. and Ivaldi G. (1989) Thermal strain analysis in the crystal structure of muscovite at 700 °C. *Eur. J. Mineral.*, 625-632.

Churakov S. V. (2013) Mobility of Na and Cs on montmorillonite surface under partially saturated conditions. *Environ. sci. technol.* **47**, 9816-9823.

Cliff R., Bond C., Butler R. and Dixon J. (2017) Geochronological challenges posed by continuously developing tectonometamorphic systems: insights from Rb/Sr mica ages from the Cycladic Blueschist Belt, Syros (Greece). *J. Metam. Geol.* **35**, 197-211.

Cole D. R. and Chakraborty S. (2001) Rates and mechanisms of isotopic exchange. *Rev. Mineral. Geochem.* **43**, 83-223.

Cosca M., Stunitz H., Bourgeix A. L. and Lee J. P. (2011) $^{40}Ar^*$ loss in experimentally deformed muscovite and biotite with implications for $^{40}Ar/^{39}Ar$ geochronology of naturally deformed rocks. *Geochim. Cosmochim. Acta* **75**, 7759-7778.

Cygan R. T., Liang J. J. and Kalinichev A. G. (2004) Molecular models of hydroxide, oxyhydroxide, and clay phases and the development of a general force field. *J. Phys. Chem. B* **108**, 1255-1266.

Cygan R. T., Greathouse J. A., Heinz H. and Kalinichev A. G. (2009) Molecular models and simulations of layered materials. *J. Mater. Chem.* **19**, 2470-2481.

Dahl P. S. (1996) The crystal-chemical basis for Ar retention in micas: inferences from interlayer partitioning and implications for geochronology. *Contrib. Miner. Petrol.* **123**, 22-39.

Di Vincenzo G., Ghiribelli B., Giorgetti G. and Palmeri R. (2001) Evidence of a close link between petrology and isotope records: constraints from SEM, EMP, TEM and in situ ^{40}Ar-^{39}Ar laser analyses on multiple generations of white micas (Lanterman Range, Antarctica). *Earth Planet. Sci. Lett.* **192**, 389-405.

Di Vincenzo G., Carosi R. and Palmeri R. (2004) The relationship between tectono-metamorphic evolution and argon isotope records in white mica: constraints from in situ ^{40}Ar-^{39}Ar laser analysis of the Variscan basement of Sardinia. *J. Petrol.* **45**, 1013-1043.

Di Vincenzo G., Tonarini S., Lombardo B., Castelli D. and Ottolini L. (2006) Comparison of ^{40}Ar-^{39}Ar and Rb-Sr data on phengites from the UHP Brossasco–Isasca Unit (Dora Maira Massif, Italy): implications for dating white mica. *J. Petrol.* **47**, 1439-1465.

Djimbi D. M., Gautheron C., Roques J., Tassan-Got L., Gerin C. and Simoni E. (2015) Impact of apatite chemical composition on (U-Th)/He thermochronometry: An atomistic point of view. *Geochim. Cosmochim. Acta* **167**, 162-176.

Dodson M. H. (1973) Closure temperature in cooling geochronological and petrological systems. *Contrib. Miner. Petrol.* **40**, 259-274.

Domingos R., Tremblay M. M., Shuster D. L. and Militzer B. (2020) Simulations and Experiments Reveal Effect of Nanopores on Helium Diffusion in Quartz. *ACS Earth Space Chem.* **4**, 1906–1912.

Dong H., Hall C. M., Peacor D. R. and Halliday A. N. (1995) Mechanisms of argon retention in clays revealed by laser ^{40}Ar-^{39}Ar dating. *Science* **267**, 355-359.

Dunlap W. (1997) Neocrystallization or cooling? ^{40}Ar/^{39}Ar ages of white micas from low-grade mylonites. *Chem. Geol.* **143**, 181-203.

Dunlap W. and Kronenberg A. (2001) Argon loss during deformation of micas: constraints from laboratory deformation experiments. *Contrib. Miner. Petrol.* **141**, 174-185.

Elphick S. and Graham C. (1988) The effect of hydrogen on oxygen diffusion in quartz: evidence for fast proton transients? *Nature* **335**, 243–245.

Farver J. R. and Yund R. A. (1990) The effect of hydrogen, oxygen, and water fugacity on oxygen diffusion in alkali feldspar. *Geochim. Cosmochim. Acta* **54**, 2953–2964.

Ferrage E., Lanson B., Michot L. J. and Robert J.-L. (2010) Hydration properties and interlayer organization of water and ions in synthetic Na-smectite with tetrahedral layer charge. Part 1. Results from X-ray diffraction profile modeling. *J. Phys. Chem. C* **114**, 4515-4526.

Frenkel D. and Smit B. (2002) *Understanding Mol. Simul.: from algorithms to applications. Second edition.* Academic Press, San Diego.

Forster M. A. and Lister G. S. (2014) $^{40}Ar/^{39}Ar$ geochronology and the diffusion of ^{39}Ar in phengite–muscovite intergrowths during step-heating experiments in vacuo. *Geol. Soc., Lond., Spec. Publ.* **378**, 117–135.

Fortier S. M. and Giletti B. J. (1991) Volume self-diffusion of oxygen in biotite, muscovite, and phlogopite micas. *Geochim. Cosmochim. Acta* **55**, 1319-1330.

Gautheron C., Djimbi D. M., Roques J., Balout H., Ketcham R. A., Simoni E., Pik R., Seydoux-Guillaume A.-M. and Tassan-Got L. (2020) A multi-method, multi-scale theoretical study of He and Ne diffusion in zircon. *Geochim. Cosmochim. Acta* **268**, 348-367.

Gerin C., Gautheron C., Oliviero E., Bachelet C., Djimbi D. M., Seydoux-Guillaume A.-M., Tassan-Got L., Sarda P., Roques J. and Garrido F. (2017) Influence of vacancy damage on He diffusion in apatite, investigated at atomic to mineralogical scales. *Geochim. Cosmochim. Acta* **197**, 87-103.

Glodny J., Bingen B., Austrheim H., Molina J. F. and Rusin A. (2002) Precise eclogitization ages deduced from Rb/Sr mineral systematics: the Maksyutov complex, Southern Urals, Russia. *Geochim. Cosmochim. Acta* **66**, 1221-1235.

Glodny J., Kühn A. and Austrheim H. (2008) Geochronology of fluid-induced eclogite and amphibolite facies metamorphic reactions in a subduction-collision system, Bergen Arcs, Norway. *Contrib. Miner. Petrol.* **156**, 27-48.

Greathouse J. A. and Cygan R. T. (2005) Molecular dynamics simulation of uranyl (VI) adsorption equilibria onto an external montmorillonite surface. *Phys. Chem. Chem. Phys.* **7**, 3580-3586.

Greathouse J. A. and Cygan R. T. (2006) Water structure and aqueous uranyl (VI) adsorption equilibria onto external surfaces of beidellite, montmorillonite, and pyrophyllite: Results from Mol. Simul.s. *Environ. sci. technol.* **40**, 3865-3871.

Halama R., Konrad-Schmolke M., Sudo M., Marschall H. R. and Wiedenbeck M. (2014) Effects of fluid-rock interaction on $^{40}Ar/^{39}Ar$ geochronology in high-pressure rocks (Sesia-Lanzo Zone, Western Alps). *Geochim. Cosmochim. Acta* **126**, 475-494.

Hames W. and Bowring S. (1994) An empirical evaluation of the argon diffusion geometry in muscovite. *Earth Planet. Sci. Lett.* **124**, 161-169.

Hames W. E. and Cheney J. (1997) On the loss of $^{40}Ar^*$ from muscovite during polymetamorphism. *Geochim. Cosmochim. Acta* **61**, 3863-3872.

Hames W. and Hodges K. (1993) Laser $^{40}Ar/^{39}Ar$ evaluation of slow cooling and episodic loss of ^{40}Ar from a sample of polymetamorphic muscovite. *Science* **261**, 1721-1723.

Hames W. E., Cheney J. T. and Tracy R. J. (2008) Single-crystal $^{40}Ar/^{39}Ar$ age variation in muscovite of the Gassetts Schist and associated gneiss, Vermont Appalachians. *Am. Mineral.* **93**, 384-395.

Hammouda T. and Cherniak D. (2000) Diffusion of Sr in fluorphlogopite determined by Rutherford backscattering spectrometry. *Earth Planet. Sci. Lett.* **178**, 339-349.

Harrison T. M., Célérier J., Aikman A. B., Hermann J. and Heizler M. T. (2009) Diffusion of ^{40}Ar in muscovite. *Geochim. Cosmochim. Acta* **73**, 1039-1051.

Hart S. R. (1960) Mineral ages and metamorphism. Ph. D. thesis, Massachusetts Institute of

Technology.

Helgeson H. C. and Aagaard P. (1985) Activity/composition relations among silicates and aqueous solutions; I, Thermodynamics of intrasite mixing and substitutional order/disorder in minerals. *Am. J. Sci.* **285**, 769-844.

Herrero C., Sanz J. and Serratosa J. (1985) Si, Al distribution in micas; analysis by high-resolution ^{29}Si NMR spectroscopy. *J. Phys. C* **18**, 13.

Herrero C., Gregorkiewitz M., Sanz J. and Serratosa J. (1987) ^{29}Si MAS-NMR spectroscopy of mica-type silicates: Observed and predicted distribution of tetrahedral Al-Si. *Phys. Chem. Miner.* **15**, 84-90.

Hess J., Lippolt H. and Wirth R. (1987) Interpretation of ^{40}Ar/^{39}Ar spectra of biotites: Evidence from hydrothermal degassing experiments and TEM studies. *Chem. Geol. (Isotope Geoscience section)* **66**, 137-149.

Hodges K. and Bowring S. (1995) ^{40}Ar/^{39}Ar thermochronology of isotopically zoned micas: Insights from the southwestern USA proterozoic orogen. *Geochim. Cosmochim. Acta* **59**, 3205-3220.

Hodges K. V., Harries W. E. and Bowring S. A. (1994) ^{40}Ar/^{39}Ar age gradients in micas from a high-temperature-low-pressure metamorphic terrain: Evidence for very slow cooling and implications for the interpretation of age spectra. *Geology* **22**, 55-58.

Ho T. A., Argyris D., Papavassiliou D. V., Striolo A., Lee L. L. and Cole D. R. (2011) Interfacial water on crystalline silica: a comparative molecular dynamics simulation study. *Mol. Simul.* **37**, 172-195.

Itaya T., Hyodo H., Tsujimori T., Wallis S., Aoya M., Kawakami T. and Gouzu C. (2009) Regional-Scale Excess Ar wave in a Barrovian type metamorphic belt, eastern Tibetan Plateau. *Island Arc* **18**, 293-305.

Jónsson H., Mills G. and Jacobsen K. W. (1998) Nudged elastic band method for finding minimum energy paths of transitions. In *Classical and Quantum Dynamics in Condensed Phase Simulations* (eds B. J. Berne, G. Ciccotti, and D. F. Coker). World Scientific, Singapore, pp.

385-404.

Kalinichev A. G., Padma Kumar P. and James Kirkpatrick R. (2010) Molecular dynamics computer simulations of the effects of hydrogen bonding on the properties of layered double hydroxides intercalated with organic acids. *Phil. Mag.* **90**, 2475-2488.

Kerisit S., Liu C. and Ilton E. S. (2008) Molecular dynamics simulations of the orthoclase (001)-and (010)-water interfaces. *Geochim. Cosmochim. Acta* **72**, 1481-1497.

Kirkpatrick R., Kalinichev A. and Wang J. (2005) Molecular dynamics modelling of hydrated mineral interlayers and surfaces: structure and dynamics. *Mineral. Mag.* **69**, 289-308.

Kirschner D. L., Cosca M. A., Masson H. and Hunziker J. C. (1996) Staircase $^{40}Ar/^{39}Ar$ spectra of fine-grained white mica: Timing and duration of deformation and empirical constraints on argon diffusion. *Geology* **24**, 747-750.

Kramar N., Cosca M. A. and Hunziker J. C. (2001) Heterogeneous $^{40}Ar^*$ distributions in naturally deformed muscovite: in situ UV-laser ablation evidence for microstructurally controlled intragrain diffusion. *Earth Planet. Sci. Lett.* **192**, 377-388.

Kramar N., Cosca M. A., Buffat P. A. and Baumgartner L. P. (2003) Stacking fault-enhanced argon diffusion in naturally deformed muscovite. *Geol. Soc., Lond., Spec. Publ.* **220**, 249-260.

Kronenberg A. K., Kirby S. H. and Pinkston J. (1990) Basal slip and mechanical anisotropy of biotite. *J. Geophys. Res. Solid Earth* **95**, 19257-19278.

Larentzos J. P., Greathouse J. A. and Cygan R. T. (2007) An ab initio and classical molecular dynamics investigation of the structural and vibrational properties of talc and pyrophyllite. *J. Phys. Chem. C* **111**, 12752-12759.

Laurent V., Scaillet S., Jolivet L., Augier R. and Roche V. (2021) ^{40}Ar behaviour and exhumation dynamics in a subduction channel from multi-scale $^{40}Ar/^{39}Ar$ systematics in phengite. *Geochim. Cosmochim. Acta* **311**, 141-173.

Lee J. K. (1995) Multipath diffusion in geochronology. *Contrib. Miner. Petrol.* **120**, 60-82.

Lister G. S. and Baldwin S. L. (1996) Modelling the effect of arbitrary PTt histories on argon diffusion in minerals using the MacArgon program for the Apple Macintosh. *Tectonophysics* **253**, 83–109.

Lister G. and Forster M. (2016) White mica $^{40}Ar/^{39}Ar$ age spectra and the timing of multiple episodes of high-P metamorphic mineral growth in the Cycladic eclogite–blueschist belt, Syros, Aegean Sea, Greece. *J. Metam. Geol.* **34**, 401–421.

Liu H., Wang L., Li S., Yang Y., Tian H., Sun F., Liu L., Li Y., Cui Y. and others (2021) A first-principles study of helium diffusion in quartz and coesite under high pressure up to 12GPa. *Geosci. Front.* **12**, 1001-1009.

Liu X., Lu X., Wang R., Zhou H. and Xu S. (2007) Interlayer structure and dynamics of alkylammonium-intercalated smectites with and without water: A molecular dynamics study. *Clays and Clay Miner.* **55**, 554-564.

Liu X., Lu X., Wang R. and Zhou H. (2008) Effects of layer-charge distribution on the thermodynamic and microscopic properties of Cs-smectite. *Geochim. Cosmochim. Acta* **72**, 1837-1847.

Livi K. J., Christidis G. E., Árkai P. and Veblen D. R. (2008) White mica domain formation: A model for paragonite, margarite, and muscovite formation during prograde metamorphism. *Am. Mineral.* **93**, 520-527.

Loewenstein W. (1954) The distribution of aluminum in the tetrahedra of silicates and aluminates. *Am. Mineral.: J. Earth Planet. Mater.* **39**, 92-96.

Loganathan N. and Kalinichev A. G. (2013) On the hydrogen bonding structure at the aqueous interface of ammonium-substituted mica: A molecular dynamics simulation. *Zeitschrift für Naturforschung A* **68**, 91-100.

Malani A., Ayappa K. and Murad S. (2009) Influence of hydrophilic surface specificity on the structural properties of confined water. *J. Phys. Chem. B* **113**, 13825-13839.

Massonne H. J. and Schreyer W. (1987) Phengite geobarometry based on the limiting assemblage with K-feldspar, phlogopite, and quartz. *Contrib. Miner. Petrol.* **96**, 212-224.

Massonne H. J. and Schreyer W. (1989) Stability field of the high-pressure assemblage, talc + phengite and two new phengite barometers. *Eur. J. Mineral.* **1**, 391-410.

McDougall I. and Harrison T. M. (1999) *Geochronology and Thermochronology by the $^{40}Ar/^{39}Ar$ Method.*, Oxford University Press, New York.

Mehrer H. (2007) *Diffusion in solids: fundamentals, methods, materials, diffusion-controlled processes.*, Springer Science & Business Media.

Meleshyn A. (2008) Two-dimensional ordering of water adsorbed on a mica surface at room temperature. *J. Phys. Chem. C* **112**, 14495-14500.

Mellini M. (1982) The crystal structure of lizardite 1T: hydrogen bonds and polytypism. *Am. Mineral.* **67**, 587-598.

Momma K. and Izumi F. (2011) VESTA 3 for three-dimensional visualization of crystal, volumetric and morphology data. *J. appl. crystal.* **44**, 1272-1276.

Monié, P. (1990) Preservation of Hercynian $^{40}Ar/^{39}Ar$ ages through high-pressure low-temperature Alpine metamorphism in the Western Alps. *Eur. J. Mineral.*, 343-361.

Monié P. and Chopin C. (1991) $^{40}Ar/^{39}Ar$ dating in coesite-bearing and associated units of the Dora Maira massif, Western Alps. *Eur. J. Mineral.*, 239-262.

Morrow C. P., Yazaydin A. Ö., Krishnan M., Bowers G. M., Kalinichev A. G. and Kirkpatrick R. J. (2013) Structure, energetics, and dynamics of smectite clay interlayer hydration: Molecular dynamics and metadynamics investigation of Na-hectorite. *J. Phys. Chem. C* **117**, 5172-5187.

Mulch A., Cosca M. and Handy M. (2002) In-situ UV-laser $^{40}Ar/^{39}Ar$ geochronology of a micaceous mylonite: an example of defect-enhanced argon loss. *Contrib. Miner. Petrol.* **142**, 738-752.

Padma Kumar P., Kalinichev A. G. and Kirkpatrick R. J. (2006) Hydration, swelling, interlayer structure, and hydrogen bonding in organolayered double hydroxides: Insights from molecular dynamics simulation of citrate-intercalated hydrotalcite. *J. Phys. Chem. B* **110**, 3841-3844.

1050 Purdy J. and Jäger E. (1976) K-Ar ages on rock forming minerals from the Central Alps. *Mem.*
1051 *1st. Geol. Min. Univ. Padova* **30**, 31.

1052 Putlitz B., Cosca M. and Schumacher J. (2005) Prograde mica $^{40}Ar/^{39}Ar$ growth ages recorded in
1053 high pressure rocks (Syros, Cyclades, Greece). *Chem. Geol.* **214**, 79-98.

1054 Putnis A. (2009) Mineral replacement reactions. *Rev. Mineral. Geochem.* **70**, 87-124.

1055 Rapaport D. C. (2004) *The art of molecular dynamics simulation.*, Cambridge university press.

1056 Robbins C. (1972) Radiogenic argon diffusion in muscovite under hydrothermal conditions. M.S.
1057 Thesis, Brown University, Providence, RI.

1058 Ruiz Pestana L., Kolluri K., Head-Gordon T. and Lammers L. N. (2017) Direct exchange mechanism
1059 for interlayer ions in non-swelling clays. *Environ. sci. technol.* **51**, 393-400.

1060 Saadoune I., Purton J. A. and de Leeuw N. H. (2009) He incorporation and diffusion pathways
1061 in pure and defective zircon $ZrSiO_4$: A density functional theory study. *Chem. Geol.* **258**,
1062 182-196.

1063 Scaillet S. (1996) Excess ^{40}Ar transport scale and mechanism in high-pressure phengites: A case
1064 study from an eclogitized metabasite of the Dora-Maira nappe, western Alps. *Geochim.*
1065 *Cosmochim. Acta* **60**, 1075-1090.

1066 Scaillet S. (1998) K-Ar ($^{40}Ar/^{39}Ar$) geochronology of ultrahigh pressure rocks. In *When continents*
1067 *collide: Geodynamics and geochemistry of ultrahigh-pressure rocks.* Springer. pp. 161-201.

1068 Scaillet S., Féraud G., Lagabrielle Y., Ballèvre M. and Ruffet G. (1990) $^{40}Ar/^{39}Ar$ laser-probe dating
1069 by step heating and spot fusion of phengites from the Dora Maira nappe of the Western Alps,
1070 Italy. *Geology* **18**, 741-744.

1071 Scaillet S., Féraud G., Ballèvre M. and Amouric M. (1992) Mg/Fe and [(Mg,Fe)Si-Al_2] compo-
1072 sitional control on argon behaviour in high-pressure white micas: A $^{40}Ar/^{39}Ar$ continuous
1073 laser-probe study from the Dora-Maira nappe of the internal Western Alps, Italy. *Geochim.*
1074 *Cosmochim. Acta* **56**, 2851-2872.

1075 Schertl H. P. and Hammerschmidt K. (2016) Tracking the incidence of excess argon in white mica
1076 Ar-Ar data from UHP conditions to upper crustal levels in the Dora-Maira Massif, Western
1077 Alps. *Eur. J. Mineral.* **28**, 1255-1275.

1078 Scibiorski E., Jourdan F., Mezger K., Tohver E. and Vollstaedt H. (2021) Cryptic excess argon
1079 in metamorphic biotite: Anomalously old $^{40}Ar/^{39}Ar$ plateau dates tested with Rb/Sr ther-
1080 mochronology and Ar diffusion modelling. *Geochim. Cosmochim. Acta* **315**, 1–23.

1081 Shau Y.-H., Feather M. E., Essene E. J. and Peacor D. R. (1991) Genesis and solvus relations of sub-
1082 microscopically intergrown paragonite and phengite in a blueschist from northern California.
1083 *Contrib. Miner. Petrol.* **106**, 367-378.

1084 Shea W. T. and Kronenberg A. K. (1992) Rheology and deformation mechanisms of an isotropic
1085 mica schist. *J. Geophys. Res. Solid Earth* **97**, 15201-15237.

1086 Spencer K., Hacker B., Kylander-Clark A., Andersen T., Cottle J., Stearns M., Poletti J. and
1087 Seward G. (2013) Campaign-style titanite U-Pb dating by laser-ablation ICP: Implications
1088 for crustal flow, phase transformations and titanite closure. *Chem. Geol.* **341**, 84-101.

1089 Szczerba M., Derkowski A., Kalinichev A. G. and Środoń J. (2015) Molecular modeling of the effects
1090 of ^{40}Ar recoil in illite particles on their K-Ar isotope dating. *Geochim. Cosmochim. Acta*
1091 **159**, 162-176.

1092 Tao L., Xiao-Feng T., Yu Z. and Tao G. (2010) Swelling of K^+, Na^+ and Ca^{2+}-montmorillonites
1093 and hydration of interlayer cations: a molecular dynamics simulation. *Chin. Phys. B* **19**,
1094 109101.

1095 Tardy Y. and Fritz B. (1981) An ideal solid solution model for calculating solubility of Clay miner..
1096 *Clay miner.* **16**, 361-373.

1097 Teich-McGoldrick S. L., Greathouse J. A. and Cygan R. T. (2012) Molecular dynamics simulations
1098 of structural and mechanical properties of muscovite: pressure and temperature effects. *J.*
1099 *Phys. Chem. C* **116**, 15099-15107.

1100 Thompson A. P., Aktulga H. M., Berger R., Bolintineanu D. S., Brown W. M., Crozier P. S.,

in 't Veld P. J., Kohlmeyer A., Moore S. G., Nguyen T. D. and others (2021) LAMMPS − a flexible simulation tool for particle-based materials modeling at the atomic, meso, and continuum scales. *Comput. Phys. Com.* **271**, 108171.

Villa I. M. (2021) The in vacuo release of Ar from minerals: 1. Hydrous minerals. *Chem. Geol.* **564**, 120076.

Villa I. M. and Puxeddu M. (1994) Geochronology of the Larderello geothermal field: new data and the "closure temperature" issue. *Contrib. Miner. Petrol.* **115**, 415-426.

Vineyard G. H. (1957) Frequency factors and isotope effects in solid state rate processes. *J. Phys. Chem. Sol.* **3**, 121-127.

Wander M. C. and Clark A. E. (2008) Structural and dielectric properties of quartz- water interfaces. *J. Phys. Chem. C* **112**, 19986-19994.

Wang G. F. and Banno S. (1987) Non-stoichiometry of interlayer cations in micas from low-to middle-grade metamorphic rocks in the Ryoke and the Sanbagawa belts, Japan. *Contrib. Miner. Petrol.* **97**, 313-319.

Wang K., Brodholt J. and Lu X. (2015) Helium diffusion in olivine based on first principles calculations. *Geochim. Cosmochim. Acta* **156**, 145-153.

Wang K., Lu X. and Brodholt J. P. (2020) Diffusion of noble gases in subduction zone hydrous minerals. *Geochim. Cosmochim. Acta* **291**, 50-61.

White, J. A. (1999) Lennard-Jones as a model for argon and test of extended renormalization group calculations. *J. Chem. Phys.* **111(20)**, 9352-9356.

Wijbrans J. R. and McDougall I. (1986) $^{40}Ar/^{39}Ar$ dating of white micas from an Alpine high-pressure metamorphic belt on Naxos (Greece): the resetting of the argon isotopic system. *Contrib. Miner. Petrol.* **93**, 187–194.

Wijbrans J. and McDougall I. (1988) Metamorphic evolution of the Attic Cycladic Metamorphic Belt on Naxos (Cyclades, Greece) utilizing $^{40}Ar/^{39}Ar$ age spectrum measurements. *J. Metam.*

Geol. **6**, 571–594.

Wunder B. and Melzer S. (2002) Interlayer vacancy characterization of synthetic phlogopitic micas by IR spectroscopy. *Eur. J. Mineral.* **14**, 1129-1138.

Yu C. J., Choe S. H., Jang Y. M., Jang G. H. and Pae Y. H. (2016) First-principles study of organically modified muscovite mica with ammonium (NH_4^+) or methylammonium ($CH_3NH_3^+$) ion. *J. Mater. Sci.* **51**, 10806-10818.

Tables

Table 1: Interaction parameters used in the simulations

Nonbonded parameters			
Atoms	Charge (e)	σ (Å)	ϵ (kcal.mol^{-1})
H (hydroxyl)[a]	0.4250	-	-
O1 (hydroxyl)[a]	-0.9500	3.1655	0.1554
O2 (bridging Oxygen)[a]	-1.0500	3.1655	0.1554
O3 (Oxygen bonded to tetrahedral Al)[a]	-1.1688	3.1655	0.1554
Al (octahedral)[a]	1.5750	4.2712	1.3298×10^{-6}
Al2 (tetrahedral)[a]	1.5750	3.3020	1.8405×10^{-6}
Si[a]	2.1000	3.3020	1.8405×10^{-6}
K[a]	1.0000	3.3340	0.1000
Ar[b]	0.0000	3.4010	0.2304

[a]Cygan et al. (2004) [b]White (1999)

Bonded parameters			
Atom 1	Atom 2	k_1 (kcal.mol^{-1}.Å^{-2})	r_0 (Å)
O1 (hydroxyl)	H (hydroxyl)	554.1349	1.0000

Table 2: Comparison of experimental and simulated crystallographic parameters of $2M_1$ Muscovite

	Experiment	MD simulations (CLAYFF)	Deviation (± %)
a (Å)	5.191	5.182	-0.17
b (Å)	9.006	8.944	-0.69
c (Å)	20.068	19.697	-1.85
α (°)	90.000	89.787	-0.24
β (°)	95.770	95.936	+0.17
γ (°)	90.000	90.175	+0.19
Interlayer sep. (Å)	3.396	3.368	-0.88

Table 3: Computed migration barriers and ^{40}Ar diffusion parameters for the monovacancy (□) and divacancy (□□) mechanisms.

	Mean energy barriers		Effective energy barriers		^{40}Ar Diffusion parameters	
	$\langle E^{\mathrm{Ar}} \rangle$ (kcal.mol^{-1})	$\langle E^{\mathrm{K}} \rangle$ (kcal.mol^{-1})	$E_{\mathrm{eff}}^{\mathrm{Ar}}$ (kcal.mol^{-1})	$E_{\mathrm{eff}}^{\mathrm{K}}$ (kcal.mol^{-1})	E (kcal.mol^{-1})	D_0 (cm^2.s^{-1})
□	71 ± 5	79 ± 9	69	75	75	4×10^{-3}
□□	69 ± 6	66 ± 10	65	58	66	6×10^{-4}

Figure captions

Fig. 1. The crystal structure atomic model of muscovite imaged with VESTA (Momma and Izumi, 2011). The system ($n = 1512$ atoms) consists of a supercell ($6 \times 3 \times 1$ unit cells) of initial dimensions $L_x = 31.146$ Å, $L_y = 27.018$ Å and $L_z = 19.966$ Å. a) Perspective view down the a axis. b) Tetrahedral layers (as labelled in (a)) showing the irregular distribution of Al atoms. Atoms are drawn with their Van der Waals radii. T_{up} and T_{low} indicate the upper and the lower tetrahedral layers with respect to the interlayer region, respectively.

Fig. 2. Variation of the energy of the system during ^{40}Ar recoil with respect to the mean energy of a system in which ^{40}Ar occupies an regular interlayer site. The red line is the running mean energy averaged over 2.5 ps. The decrease of the energy at 50 ps corresponds to the move of ^{40}Ar from the interstitial site to the lattice stable site.

Fig. 3. Geometry of diffusion in the muscovite interlayer plane. a) Monovacancy mechanism. b) Divacancy mechanism. Orange and green circles correspond to K^+ and ^{40}Ar atoms respectively. □ represents the vacancy, $\overrightarrow{V_i}$ are the displacement vectors and $\overrightarrow{\delta_i}$ indicate atomic jumps preserving the divacancy. See text for discussion.

Fig. 4. Results of NEB calculations of ^{40}Ar migration in muscovite. a) Histogram of migration barriers associated with a monovacancy mechanism. b) Histogram of migration barriers associated with a divacancy mechanism. c) Variation of the potential energy of ^{40}Ar along its path towards a monovacancy (black) and towards a vacancy pair (blue). d) Trajectories followed by ^{40}Ar as it migrates from a stable site towards a single vacancy (black) and towards a vacancy pair (blue). Red circles represent basal oxygens. e) Diagram showing the anticorrelation between the ^{40}Ar migration barriers and the total electrostatic energy of the structure.

Fig. 5. Results of NEB calculations of K^+ migration in muscovite. a) Histogram of migration barriers associated with a monovacancy mechanism. b) Histogram of migration barri-

ers associated with a divacancy mechanism. c) Variation of the potential energy of K^+ along its path towards a monovacancy (black) and towards a vacancy pair (blue). d) Trajectories followed by K^+ as it migrates from a stable site towards a single vacancy (black) and towards a vacancy pair (blue). Red circles represent basal oxygens. e) Diagram showing the positive correlation between the ^{40}Ar and K^+ migration barriers.

Fig. 6. Arrhenius plot of ^{40}Ar diffusion coefficients calculated for the monovacancy and the divacancy mechanisms. Results of previous studies are also reported for comparison.

Fig. 7. Nominal variations in $^{40}Ar-$muscovite closure temperature (Eq (1) in text) with cooling rate and grain size. T_c are calculated for a cylindrical geometry ($A = 27$), using diffusion parameters deduced from Molecular Dynamics and Transition State Theory ($E = 66$ kcal.mol^{-1}; $D_0 = 6 \times 10^{-4}$ cm^2.s^{-1}). See text for discussion.

1177 **Figures**

Fig. 1

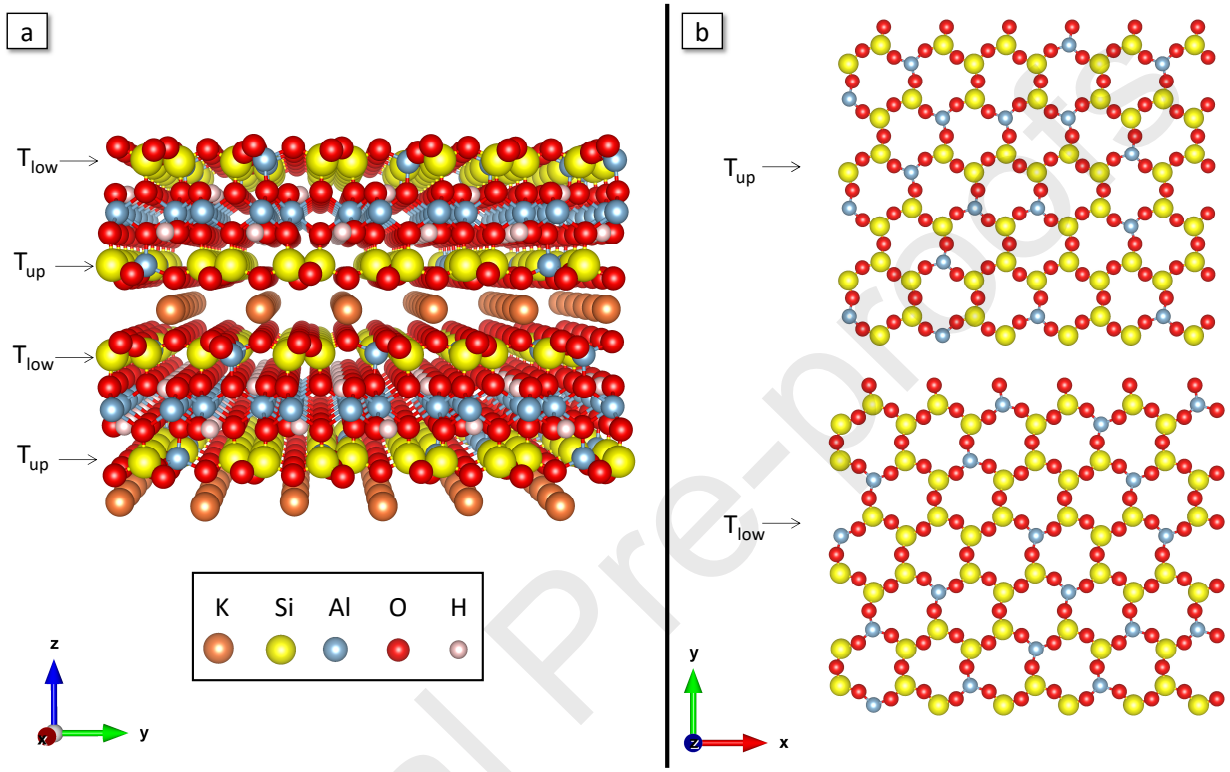

Fig. 2

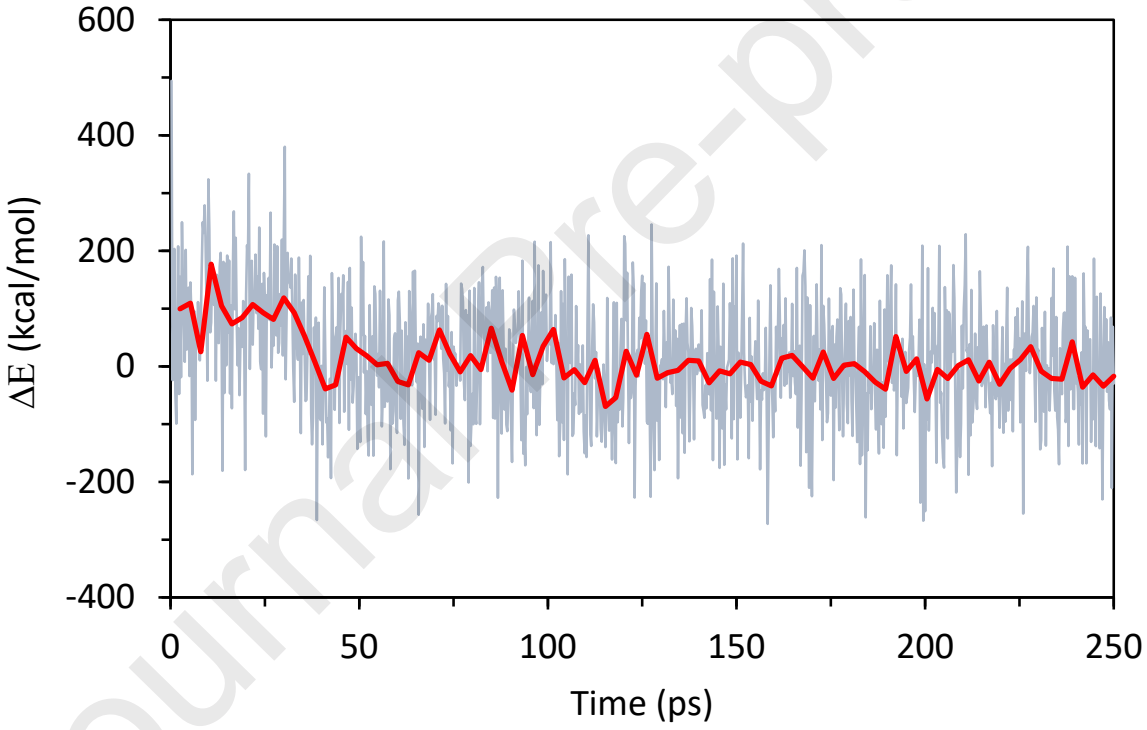

Fig. 3

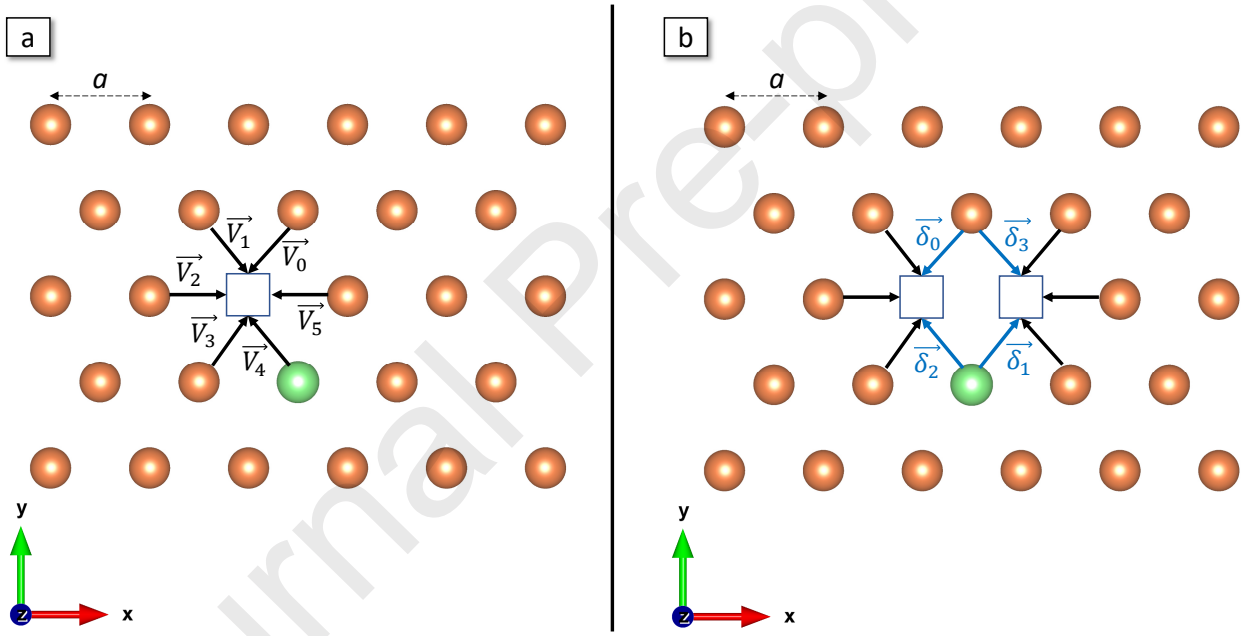

Fig. 4

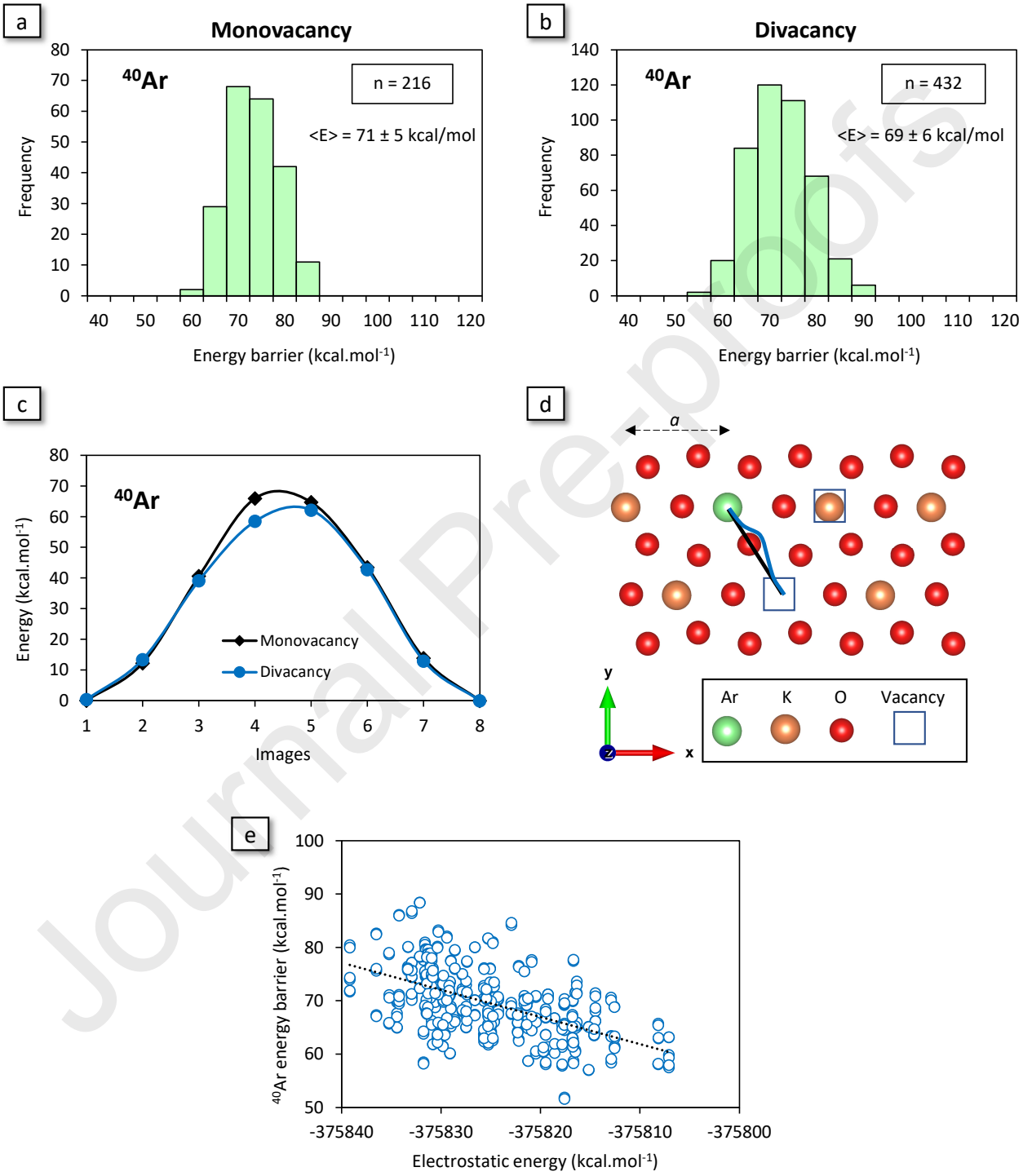

Fig. 5

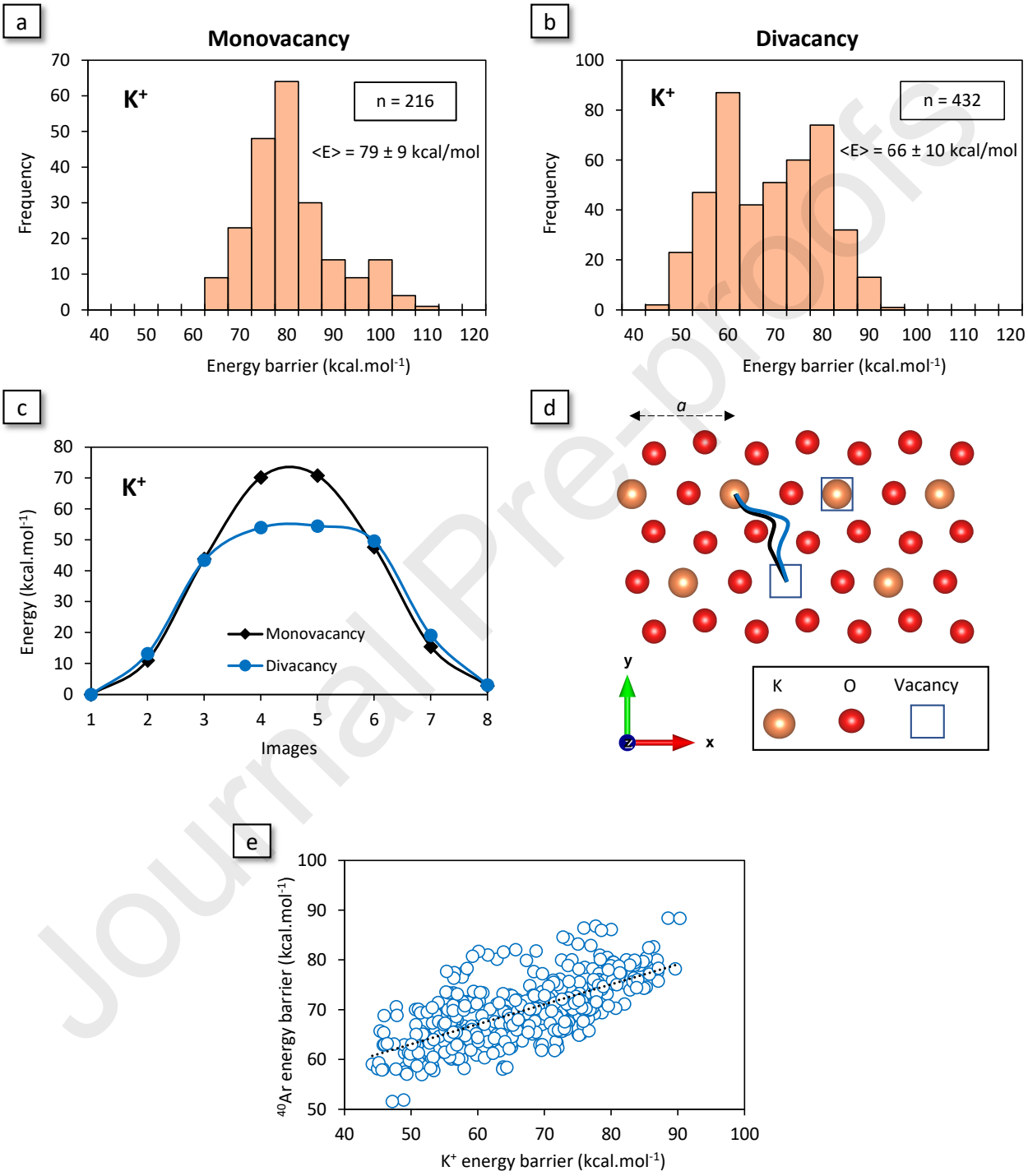

Fig. 6

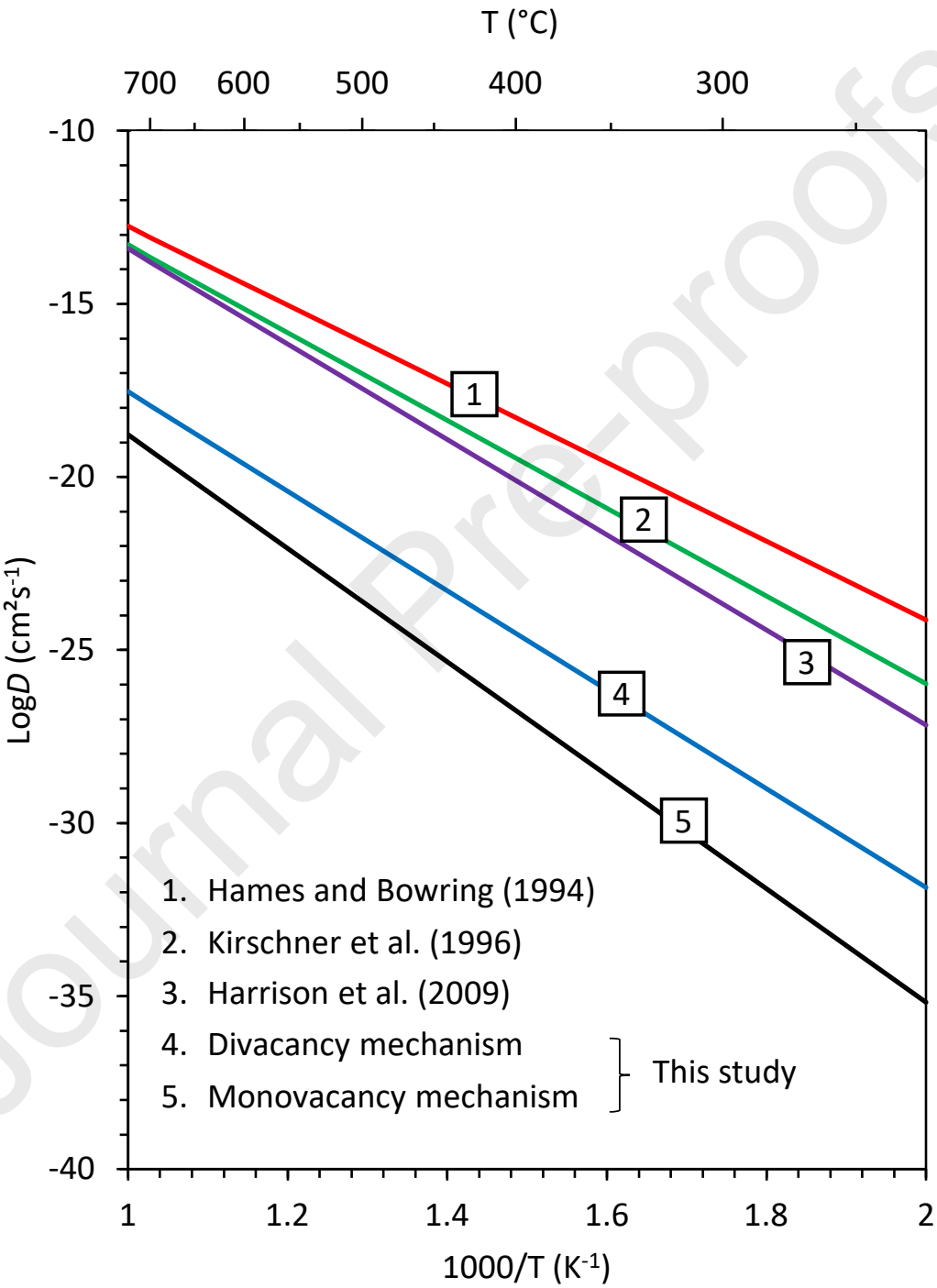

Fig. 7

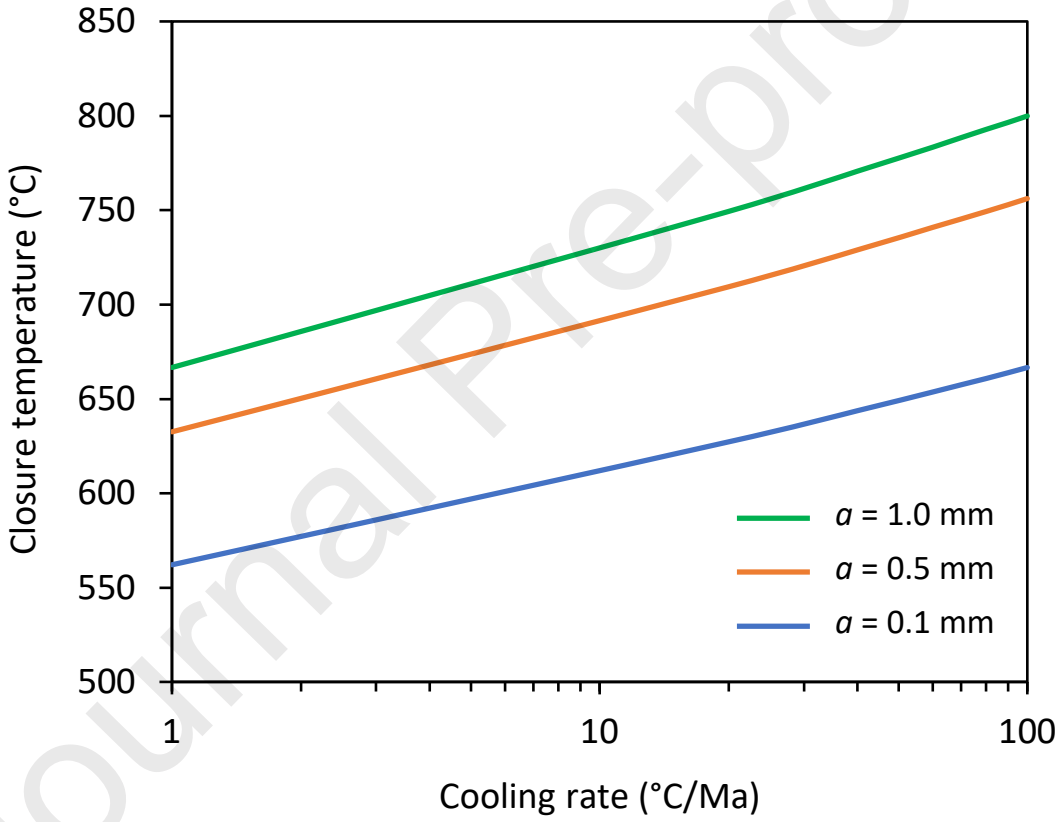

Declaration of interests

☒ The authors declare that they have no known competing financial interests or personal relationships that could have appeared to influence the work reported in this paper.

☐The authors declare the following financial interests/personal relationships which may be considered as potential competing interests: